VYSOKÉ UČENÍ TECHNICKÉ V BRNĚ
BRNO UNIVERSITY OF TECHNOLOGY

FAKULTA STROJNÍHO INŽENÝRSTVÍ
ÚSTAV FYZIKÁLNÍHO INŽENÝRSTVÍ

FACULTY OF MECHANICAL ENGINEERING
INSTITUTE OF PHYSICAL ENGINEERING

VYŽITÍ PLAZMONIKY V ORGANICKÉ FOTOVOLTAICE

APPLICATION OF PLASMONICS IN ORGANIC PHOTOVOLTAICS

DIPLOMOVÁ PRÁCE
MASTER'S THESIS

AUTOR PRÁCE **Bc. MARTIN LÁSKA**
AUTHOR

VEDOUCÍ PRÁCE **Prof. RNDr. TOMÁŠ ŠIKOLA, CSc.**
SUPERVISOR

BRNO 2011

Abstrakt
Tato diplomová práce se zabývá možností využití plasmonicky navýšené absorpce pro zlepšení účinnosti organických solárních článků. K navýšení absorpce světla ve fotoaktivní vrstvě jsou použity koloidní nanočástice stříbra. Rozptyl světla z nanočástic stříbra do fotoaktivní vrstvy představuje jedno z možných řešení, jak navýšit celkovou účinnost fotovoltaických zařízení. Simulace elektromagnetických jevů jsou pro statické podmínky prováděny použitím softwaru Lumerical (Lumerical Solutions, Inc.). Je zkoumána absorpce i rozptyl ve fotoaktivní vrstvě v závislosti na konfiguraci stříbrných nanočástic. Simulace potvrzují, že ve fotoaktivní vrstvě, která je modifikovaná nanočásticemi stříbra, dochází k navýšení absorpce. Abychom experimentálně potvrdili výsledky simulací, bylo vyrobeno několik stříbrem modifikovaných vzorků. Vzorky byly pro tento druh experimentu připravené z poly(3-hexyltiofenu):[6,6]-fenyl-C_{61}-butyric-acid-metyl esteru. U některých nanočásticemi stříbra modifikovaných vzorků dochází k navýšení tvorby excitonů, v důsledku čehož je pozorován nárůst fotoproudu. V této práci je zahrnut teoretický i experimentální přístup k dané problematice.

Summary
The diploma thesis deals with the application of the plasmon-enhanced absorption to an improvement of the power conversion efficiency in organic solar cells. To increase the light absorption in the photoactive layer, colloidal silver nanoparticles are used. The scattering of the light from silver nanoparticles into a photoactive layer represents one of possible solutions how to increase the power conversion efficiency of photovoltaic devices. To perform electromagnetic simulations in the steady-state regime, the software Lumerical (Lumerical Solutions, Inc.), has been used. For different geometrical arrangements of silver nanoparticles, the absorption and the scattering in the photoactive layer is observed. Simulations prove the enhancement of the absorption in the photoactive layer while incorporating silver nanoparticles. To experimentally confirm results from these simulations, a couple of samples modified with silver nanoparticles, was prepared. The samples produced for this kind of experiments are based on Poly(3-hexylthiophene):[6,6]-Phenyl-C_{61}-butyric-acid-methyl ester. For some samples modified with silver nanoparticles, an exciton creation has been improved. As the result, the enhancement in the short-circuit current is observable. The thesis covers both the theoretical and experimental approach to this topic.

Klíčová slova
Organické solární články, plasmonicky navýšená absorpce, P3HT:$PCBM_{(60)}$, nanočástice stříbra, optické vlastnosti.

Keywords
Organic solar cells, plasmon-enhanced absorption, P3HT:$PCBM_{(60)}$, silver nanoparticles, optical properties.

LÁSKA, M. *Využití plazmoniky v organické fotovoltaice*. Brno: Vysoké učení technické v Brně, fakulta strojního inženýrství, 2011. 72 s. Vedoucí diplomové práce Prof. RNDr. Tomáš Šikola, CSc.

Prohlášení

Prohlašuji, že jsem tuto diplomovou práci vypracoval samostatně, pod odborným vedením Prof. RNDr. Tomáše Šikoly, CSc., a že veškeré podklady, ze kterých jsem čerpal, jsou uvedeny v seznamu použité literatury.

V Brně 27. května 2011

Poděkování

Na tomto místě bych rád poděkoval prof. RNDr. Tomáši Šikolovi, CSc. za konzultace a připomínky během tvorby této diplomové práce, prof. dr. ir. Renému A. J. Janssenovi z Technické univerzity v Eindhovenu (Holandsko), který mi poskytnul technické zázemí pro přípravu potřebných vzorků. Dále děkuji Ing. Lukáši Břínkovi, který svými připomínkami napomohl moji práci zkvalitnit. V neposlední řadě děkuji své rodině za podporu během studia a v životě.

CONTENTS

1. INTRODUCTION **13**

2. FUNDAMENTALS OF ORGANIC PHOTOVOLTAICS **15**

3. PLASMONICS IN ORGANIC PHOTOVOLTAICS **21**
3.1. Plasmon-enhanced absorption 21
3.2. Joule heating 22
3.3. Light scattering 24

4. ELECTROMAGNETIC SIMULATIONS **29**
4.1. Finite-Difference Time Domain method 29
4.2. Results of simulations 31
4.2.1. Ag nanoparticles positionned on the PEDOT:PSS - ITO interface 33
4.2.2. Ag nanoparticles positionned in P3HT:$PCBM_{(60)}$ 36
4.2.3. Ag nanoparticles positionned on the PEDOT:PSS - ITO interface and in P3HT:$PCBM_{(60)}$ 39

5. EXPERIMENTAL SECTION **43**
5.1. Device fabrication 43
5.1.1. Fabrication of reference samples 44
5.1.2. Fabrication of samples modified with Ag nanoparticles - Spin-coating method 46
5.1.3. Fabrication of samples modified with Ag nanoparticles - Drop-casting method 50
5.1.4. Fabrication of samples with deposited Ag nanoaprticles 51
5.2. Measurement technique 55
5.2.1. Volt-amper characteristic measurements (*I-U*) 55
5.2.2. External quantum efficiency measurements (*EQE*) 59
5.2.3. Steady-state differential current measurements (*SSDC*) 61
5.2.4. Layer thickness measurements 63
5.2.5. Atomic force microscopy measurements (*AFM*) 65

6. CONCLUSION **67**

BIBLIOGRAPHY 71

1. INTRODUCTION

Harvesting the energy directly from the sunlight using photovoltaic technology is widely recognized as an essential component for future global energy production. The worldwide photovoltaic production was more than 5 GW in 2008, and is expected to rise above 20 GW by 2015. Photovoltaics could make a considerable contribution to solving the energy problem that the human society faces nowadays. Recently, it has been shown that inorganic components in the photovoltaics can be replaced by semiconducting polymers. These solar cells based on organic materials have gained a considerable interest due to its application versatility, and cost-effective processes such as high-throughput roll-to-roll systems. Bulk-heterojunction (*BHJ*) cells, where donor and acceptor materials are blended together, are promising as an inexpensive alternative to conventional inorganic based photovoltaic cells. Nevertheless, the power conversion efficiency of organic photovoltaic systems still need to be improved (8% [1] vs 40% for silicon multijunction solar cells [2]). To improve the efficiency of plastic solar cells, it is, therefore, crucial to understand what limits their performance. Light absorption is one of significant limiting factors to the efficiency of the organic photovoltaics (*OPV*). Using the plasmonics to enhance the absorption in *OPV* seems to be a promising solution. Plasmonics is a relatively new discipline, which deals with collective oscillations of electrons at metallic surfaces. It has been shown that the enhancement of the absorption in the photoactive layer is strongly dependent on the position and geometry of incorporated metal nanostructures [3]. The light absorption of such modified conjugated polymer cells is supposed to increase by reason of the enhanced localized electric field in the vicinity of nanostructures. In this work, an effort to enhance the absorption in photoactive layer in organic solar cells based on Poly(3-hexylthiophene):[6,6]-Phenyl-C_{61}-butyric-acid-methyl ester (P3HT:$PCBM_{(60)}$) is made. The P3HT:$PCBM_{(60)}$ system was chosen for its proven efficiency and its ease of fabrication. For this purpose, different geometrical arrangements of silver nanoparticles with different sizes are taken into account.

The fundamentals of the organic photovoltaics are mentionned in Chapter 2 and the theoretical approach to plasmonics used in bulk heterojunction solar cells is described in Chapter 3. To perform electrostatic simulations, the software Lumerical (Lumerical Solutions, Inc.) has been used. This part is discussed in Chapter 4. Chapter 5 is devoted to the experimental section. Therefore, the fabrication and the measurement of the samples based on P3HT:$PCBM_{(60)}$ is presented here. These devices are modified with colloidal 20-nm Ag nanoparticles.

2. FUNDAMENTALS OF ORGANIC PHOTOVOLTAICS

A revolutionary development in organic photovoltaics came in the 1990s when the fullerene was used in polymers. There are many types of fullerenes differing by number of carbon atoms. Molecules of C_{60} and C_{70} (figure 1a and 1b) are the most familiar among fullerenes. Even if molecules of C_{60} and C_{70} differ only by 10 carbon atoms, their physical properties are crushingly different. For example, the molecule of C_{70} exhibits a higher external quantum efficiency (*EQE*) which is linked to the absorption for different wavelengths (figure 3). The *EQE* method will be discussed in the section 5.2.2. In principle, fullerenes are symmetric macromolecules based on alternating single and double bonds between carbon atoms. In the backbone of such conjugated macromolecules, each carbon atom binds to only two adjacent atoms, leaving one free electron per carbon atom (figure 1c) [3].

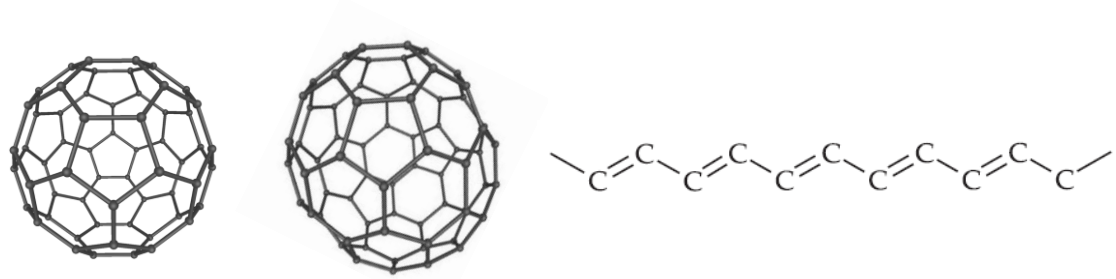

a) b) c)

Figure 1 Molecule of fullerene containig **a)** 60 carbon atoms and **b)** 70 carbon atoms [4]. **c)** Double bonds presented in a macromolecule of fullerene.

The architecture of organic solar cells is based on the bulk heterojunction where the electron donor (blue color) and electron acceptor (red color) material are blended together (figure 2).

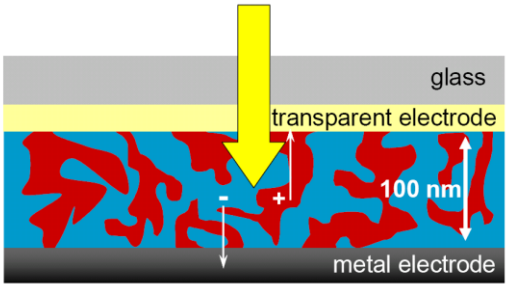

Figure 2. Structure of bulk-heterojunction solar cells [5].

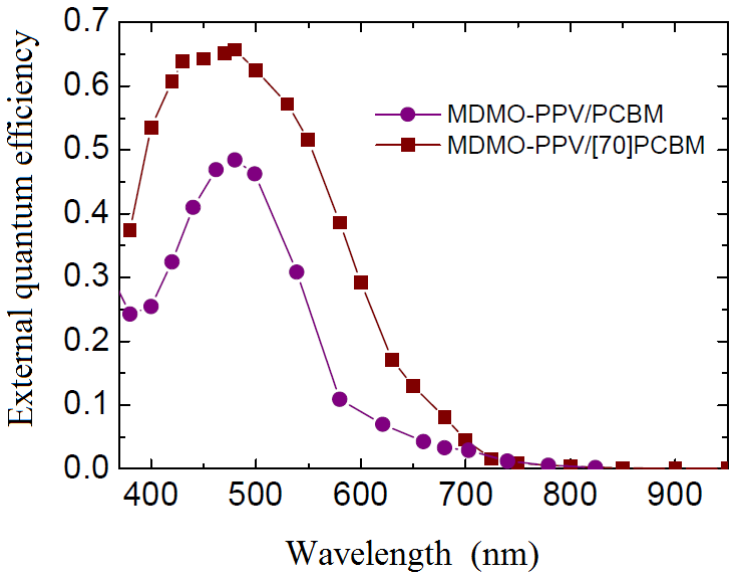

Figure 3. *EQE* of molecules C_{60} and C_{70}. The macromolecule of C_{70} exhibits a higher absorbtion compared to the macromolecule of C_{60} [5].

Conjugated polymers, as a new class of materials used in the bulk-heterojunction photovoltaics, have attracted a considerable attention due to its ease of processing and the potential of providing environmentally safe, flexible, lightweight and inexpensive electronics. Solar cells based on polymer materials commonly utilize two different substances that differ by electron donating and accepting properties. The two component blend enables a large interfacial area for the electric charge separation. Charges are created by a photoinduced electron transfer between these two components. This electron transfer between donor and acceptor boosts the photogeneration of free charge carriers. In blended materials, the formation of bound electron-hole pairs, or excitons is generally favored [3]. Compared to organic semiconductors, the inorganic ones have generally higher dielectric constants $(\varepsilon', \varepsilon'')$ and the lower exciton binding energy (E_B) (table 1).

	n	k	ε'	ε''	E_B (eV)
GaAs	4.124	0.302	16.916	2.491	0.004
P3HT:PCBM$_{(60)}$	1.961	0.263	3.776	1.032	4.1

Table 1. Optical constants and exciton binding energy for GaAs and P3HT:PCBM$_{(60)}$ (1:1) dissolved in 1,2-dichlorobenzene. The values are measured under normal conditions and for the wavelength about 532 nm [6], [7].

Samples being used in this work are composed of glass, indium tin oxide (ITO) (electrode for collecting positive charges), poly(3,4-ethylenedioxythiophene) poly (styrenesulfonate) (PEDOT:PSS) (transfering of positive charges), active layer (exciton creation and its dissociation into positive and negative charge carriers), lithium fluoride (LiF) that transfers negative charges and ensures a good adhesion between photoactive layer and Al electrode where negative charge carriers are collected. Individual organic molecular structures of fullerene bulk heterojunction solar cells based on the *PV* active layer P3HT: PCBM$_{(60)}$ are illustrated in figure 4. A simplified schematic layout of such a device architecture is shown in figure 5.

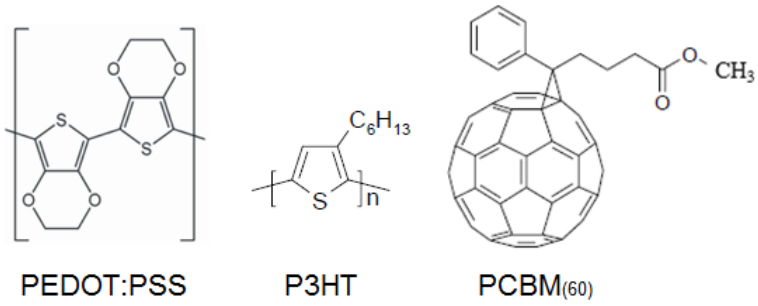

Figure 4. Molecular structures of PEDOT:PSS, P3HT (electron donor) and $PCBM_{(60)}$ (electron acceptor).

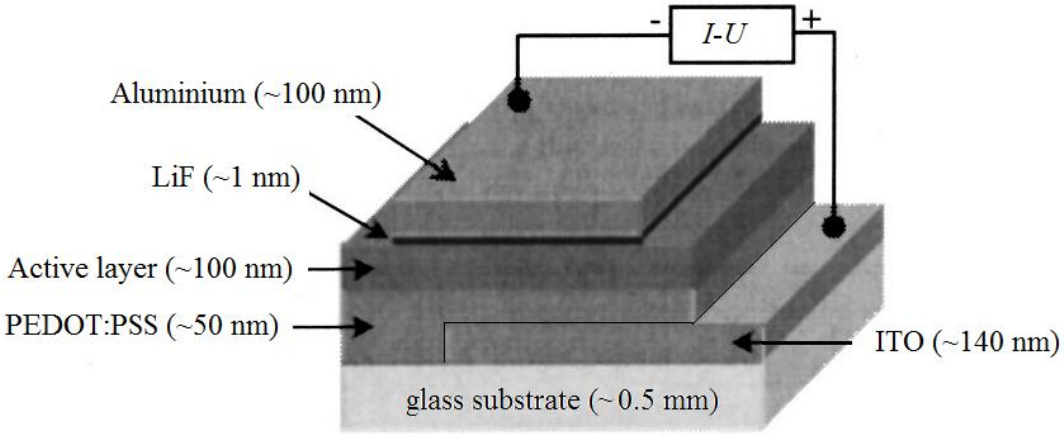

Figure 5. A simplified architecture of the solar cell based on polymer materials [3].

In principle, for an organic photovoltaic cell, four important steps take place during the conversion of the solar energy into the electrical energy:

- Absorption of light
- Exciton creation and separation of opposite charges
- Charge transport
- Charge collection

For an efficient absorption of photons, the absorption spectrum of the photoactive organic layer should match the solar emission spectrum. The photoactive layer is supposed to be sufficiently thick to absorb all the incident light. Compared to inorganic based solar cells, polymer based devices have higher optical absorption coefficients that offer the possibility to produce very thin solar cells. The energy difference between the highest occupied molecular orbital (HOMO) and the lowest unoccupied molecular orbital (LUMO) describes the excitability of the molecule. It is possible to promote an electron from HOMO to LUMO level, for example by light absorption. Creation of charges is one of key steps in photovoltaic devices. In most organic solar cells, charges are created by photoinduced electron transfer. For an efficient charge generation, it is important that after photoexcitation, the thermodynamically and kinetically most feasible pathway is the charge-separated state. As well, it is important that the charge-separated state is stabilized, so that photogenerated charges could migrate to electrodes. Otherwise, opposite charges recombine together at creating the exciton. This phenome-

non is called the bimolecular recombination. In this case, it is not possible to transport separated charges to electrodes any more. After the charge transfer, photogenerated charges are desired to migrate to these electrodes without any recombination losses, if possible. Losses during the transfer of free charge carriers present the fundamental parameter which affects the total efficiency of devices. Basic processes in *OPV* are described in figure 6 [3].

Figure 6. Principle of organic photovoltaics (*OPV*): Part (a) shows the process of light absorption by the polymer yielding an exciton which has to diffuse to the donor/acceptor interface. If the exciton reaches this interface, electron transfer to the acceptor phase is energetically favored, as shown in part (b), yielding an electron-hole pair bound by Coulombical interactions. The dissociation of the electron-hole pair, either phonon- or field assisted, produces free charge carriers, as depicted in (c). Finally, free carriers have to be transported through their respective phases to the electrodes in order to be extracted (d). Exciton decay is one possible loss mechanism, see part (e), while geminate recombination of the bound electron-hole pair and bimolecular recombination of free charge carriers (f) are two other possibilities [3].

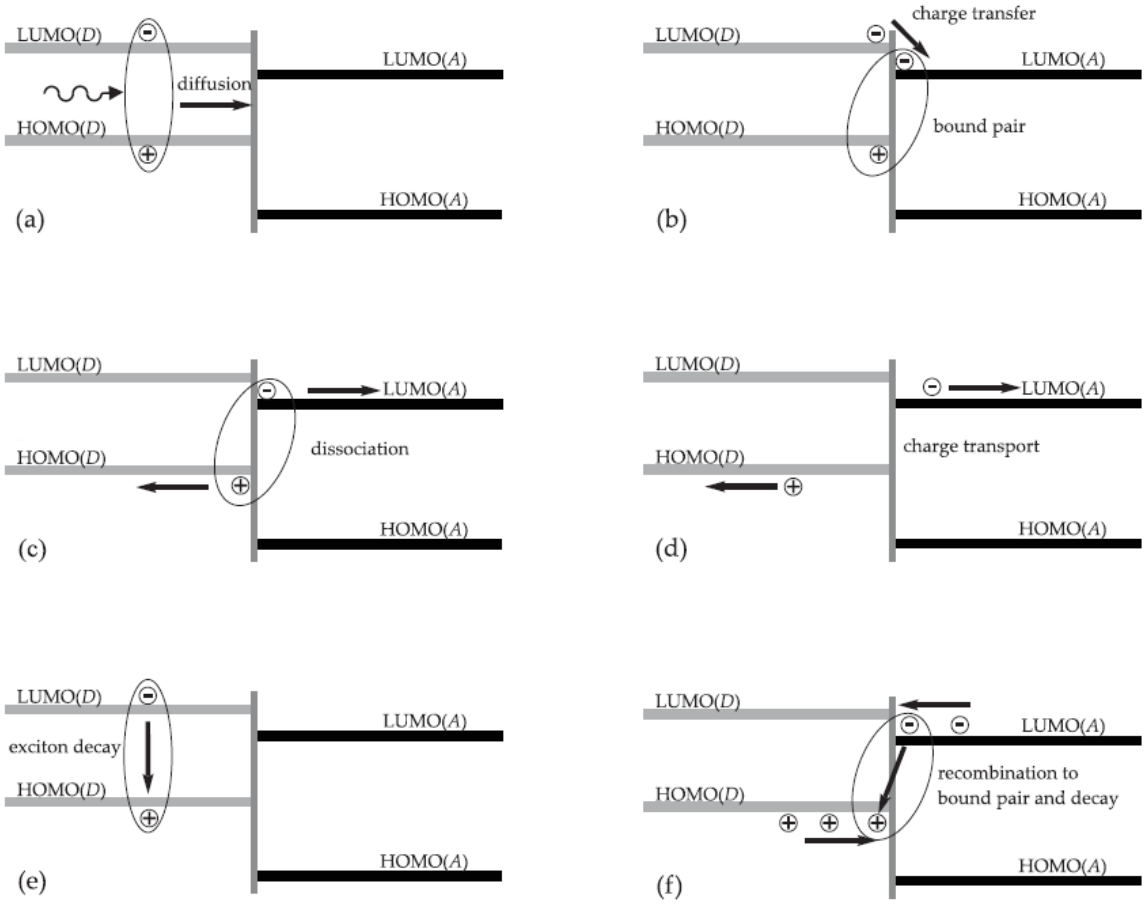

The bimolecular recombination in two different phase materials is characterized by the recombination constant k_r (equation 1) [3].

$$k_r = \frac{q}{\varepsilon}(\mu_e + \mu_h), \tag{1}$$

where q is the elementary charge, ε is the dielectric constant of the photoactive material and μ is the hole or the electron mobility, respectively. This equation is derived from the Langevin dynamics [3].

In P3HT:PCBM$_{(60)}$ blends, it is the electron mobility that dominates over the hole mobility. After annealing, the electron mobility is typically varying from ~ 10^{-8} to ~ 3×10^{-7} $m^2V^{-1}s^{-1}$ and the hole mobility in the P3HT phase increases more than three orders of magnitude to ~ 2×10^{-8} $m^2V^{-1}s^{-1}$ (figure 7). This is used to be explained as the result of the improved crystallinity of the film after annealing [8]. Moreover, upon annealing, the absorption spectrum of P3HT:PCBM$_{(60)}$ blends undergoes a strong red-shift, improving the spectral overlap with the solar emission. As the result, an increase about 60% in the generation rate of charge carriers is observed.

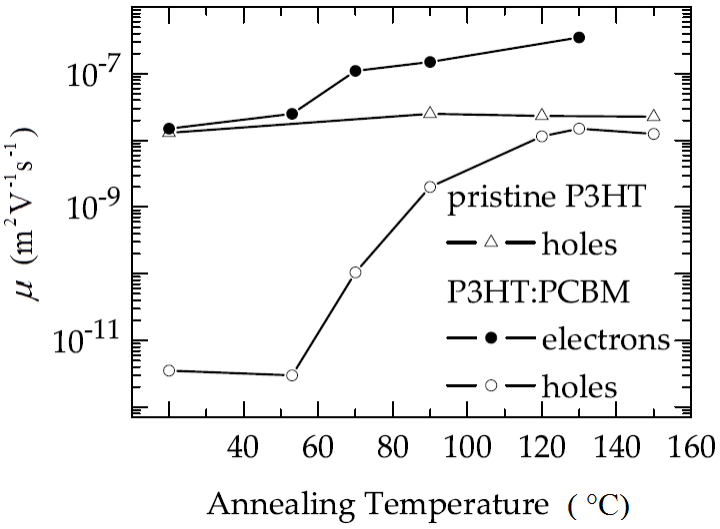

Figure 7. Electron and hole mobility in a blend of P3HT:PCBM$_{(60)}$ as a function of the annealing temperature [3].

The morphology of the active layer is the very important factor which significantly influences losses in the device during the charge transfer. The exciton, created after the light absorption, has to diffuse towards the interface for the charge separation to occur. The exciton diffusion length in P3HT:PCBM$_{(60)}$ based devices is about 15 nm. This means that for efficient charge generation after the light absorption, each exciton has to find a donor-acceptor interface within a few nanometers, otherwise it will be lost without any charge generation. Simply, it is desirable to suppress bimolecular recombinations prior to the charge generation. The control of the morphology is required not only to suppress exciton losses, but also to ensure the percolation pathway for both electron and hole transport to electrodes.

3. PLASMONICS IN ORGANIC PHOTOVOLTAICS

This chapter is devoted to fundamental principles of plasmonics used in organic photovoltaics. It is not the subject of this chapter to describe plasmonics in details because the detailed insight into this thopic is given elsewhere [10], [28], [29]. Plasmonics represents a promising tool that can help us to better understand the physical effects that occur around nanoparticles embedded in a material while illuminating. Ideally, the absorbing layer in photovoltaic device should be physically thin to provide versatile applications. On the other hand, the absorbing layer is required to be sufficiently thick to allow the light absorption. Plasmonic structures represent one of possible ways how to reduce the physical thickness of the photoactive layer while keeping their optical thickness constant. Metallic nanoparticles can be used as subwavelength antennas in which the plasmonic near-field is coupled, increasing its effective absorption cross-section. Nanoparticle dimensions are supposed to be much smaller than the light wavelength. The light scattering from a metal nanoparticle embedded in a homogeneous medium is nearly symmetric in forward and reverse directions. In addition, if the cell has a reflecting metal back contact (as in case of polymer based photovoltaic systems), the light reflected towards the surface will couple to nanoparticles and will be partly reradiated into the photoactive layer by the same scattering mechanism. As the result, the incident light will pass several times through that layer, increasing the effective path length. The effect of the particle scattering concept has been studied by several research groups [10], [16]. It is worth noting that both the size and geometrical arrangement of metal nanoparticles are the key factors that determine the scattering effect. Although, it is necesarry to take into account the thickness and physical properties of all layers in the polymer photovoltaic device.

3.1. Plasmon enhanced absorption

Metal nanoparticles show unique optical properties and strong enhancement in the electromagnetic field in their vicinity. This optical phenomenon is known as the localized surface plasmon resonance (LSPR) which is observable for several metals, for instance Au, Al, Cu or Ag. Surface plasmons are well described as confined electromagnetic waves that propagate along the conducting surface of a metal or along a metal-dielectric interface [11]. Metals show this behaviour because of the presence of free charge carriers. In this work, we use Ag nanoparticles of different sizes and geometrical arrangements to enhance the absorption in their neighborhood. Ag nanoparticles show two absorption bands at wavelengths: one at 368 nm and the other at 420 nm [12]. For Ag nanoparticles the extinction (scattering plus absorption) becomes more red shifted with increasing their size [14]. The enhanced absorption of the photoactive layer via the strong local electromagnetic field in the vicinity of Ag nanoparticles leads to an increase in the exciton creation [15] (figure 8). The external quantum efficiency method (*EQE*) proves, that in the spectral range of 330-650 nm, P3HT:$PCBM_{(60)}$ blend absorbs most of the light. Furthermore, Ag nanoparticles exhibit strong scattering effects while introdu-

cing into the photoactive layer. This also contributes to the absorption in the photoactive layer. Further, Ag nanoparticles immersed in the photoactive layer cause the enhancement in the charge carrier mobility which leads to the increased short-circuit current I_{sc} [15].

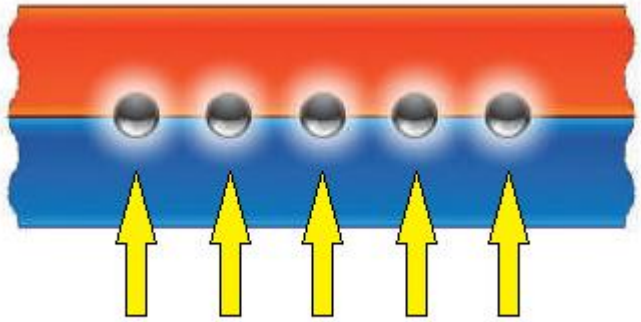

Figure 8. Light trapping by the excitation of localized surface plasmons in metal nanoparticles positionned at the interface of two semiconductors. The near-field of excited metal nanoparticles causes the creation of electron-hole pairs [15].

It has been demonstrated that at plasmon resonance wavelengths, more current is generated [3]. This results in a strong increase of the external quantum efficiency. *EQE* of thin film organic solar cells is limited by low carrier mobilities. In time-of-flight (*TOF*) experiments, the mobility μ of carriers in the polymer of our interest, can empirically be described by [3]

$$\mu = \mu_0 \exp\left(\gamma\sqrt{F}\right), \tag{2}$$

where μ_0 is the zero-field mobility, γ is the field activation parameter and F is the field strength. The thinner film between electrodes will lower the probability to bimolecular recombinations and will increase the charge carrier drift velocity by the higher electric field.

3.2. Joule heating

Another effect, that also significantly affects the absorption in the photoactive material, is generating the heat around the metal nanoparticle upon illuminating [16], [17]. The Joule heating effect is minimized for the lower particle density or the smaller particle size. The heating effect is especially strong for metal nanoparticles as they have many mobile electrons. Since metal nanoparticles show a low light emission, the total amount of the generated heat can be estimated as the total optical extinction. It has been shown that Ag nanoparticles can efficiently release the heat resulting from the optical excitation. Thus, the heat diffuses away from nanoparticles to the surrounding medium. For conditions in the steady-state regime, the temperature distribution around an optically-stimulated metal nanoparticle can be described by the usual heat transfer equation [17]:

$$\rho(r)c(r)\frac{\partial T(r,t)}{\partial t} = \nabla k(r)\nabla T(r,t) + Q(r,t), \tag{3}$$

where $\boldsymbol{r}$ is the vector of spacial coordinates, t is the time, $T(r,t)$ is the local temperature, and the material parameters $\rho(r)$, $c(r)$ and $k(r)$ express the mass density, the specific heat, and the thermal conductivity, respectively. The function $Q(r,t)$ represents an energy source coming from the light dissipation in nanoparticles. In the steady-state regime, the local temperature around a single nanoparticle can be described by the equation:

$$\Delta T(\mathrm{r}) = \frac{V_{\mathrm{NP}} Q}{4\pi k_0 r}, \tag{4}$$

where $r > R_{\mathrm{NP}}$ is the distance from the center of the metal nanoparticle of the diameter R_{NP}, k_0 is the thermal conductivity of the surrounding medium and V_{NP} is the volume of the metal nanoparticle. Assuming that the wavelength of the incident radiation is much longer than the nanoparticle radius R_{NP}, we can calculate the nanoparticle heat generation Q [17] as

$$Q = \frac{\omega}{8\pi} E_0^2 \left| \frac{3\varepsilon_0}{2\varepsilon_0 + \varepsilon_{\mathrm{NP}}} \right|^2 \mathrm{Im}\,\varepsilon_{\mathrm{NP}}, \tag{5}$$

where E_0 is the amplitude of the incident radiation, $\varepsilon_{\mathrm{NP}}$ and ε_0 are the dielectric constants of the metal nanoparticle and the surrounding medium, respectively. Here, $\varepsilon_{\mathrm{NP}}$ and ε_0 are represented in the complex form $\varepsilon_{\mathrm{NP}} = \varepsilon'_{\mathrm{NP}} + \mathrm{i}\varepsilon''_{\mathrm{NP}}$, $\varepsilon_0 = \varepsilon'_0 + \mathrm{i}\varepsilon''_0$ respectively.

The maximum enhancement in the temperature occurs at $r = R_{\mathrm{NP}}$ and is given by:

$$\Delta T_{\max}(I_0) = \frac{R_{\mathrm{NP}}^2}{3k_0} \left| \frac{3\varepsilon_0}{2\varepsilon_0 + \varepsilon_{\mathrm{NP}}} \right|^2 \frac{\omega I_0}{c\sqrt{\varepsilon_0}} \mathrm{Im}\,\varepsilon_{\mathrm{NP}}, \tag{6}$$

where I_0 is the incoming light intensity and k_0 is the thermal conductivity of the surrounding medium. This equation describes an important dependence of the temperature increase around a nanoparticle on the incoming light intensity and on the nanoparticle size.

$$\Delta T_{\max} = \Delta T\left(R_{\mathrm{NP}}^2, I_0\right) \tag{7}$$

The local temperature distribution around a 20-nm Ag nanoparticle at a plasmon resonance is illustrated in figure 9. The incoming light intensity is about 1000 W/m^2 and the coefficient of the thermal conductivity k_0 of the surrounding material (P3HT:PCBM$_{(60)}$) is well approximated by the value 1.4.

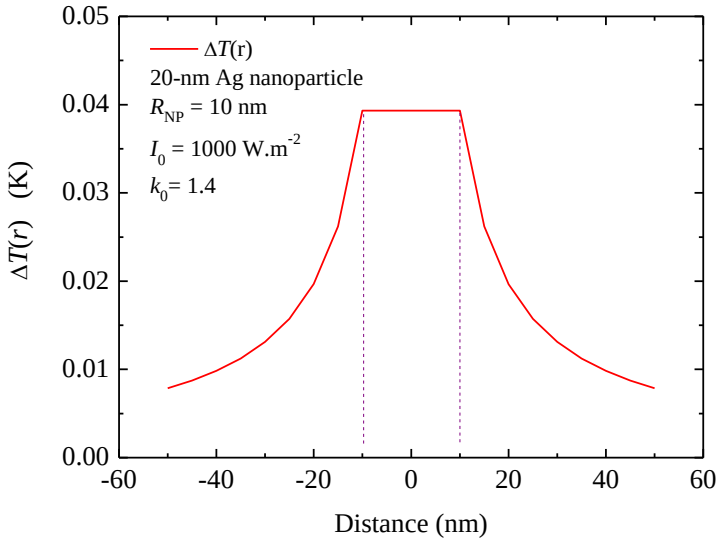

Figure 9. Temperature enhancement for a single 20-nm Ag nanoparticle in the steady-state regime as a function of the nanoparticle center distance. The surrounding medium is P3HT:PCBM$_{(60)}$ (1:1), dissolved in 1,2-dichlorobenzene.

The total heat dissipation from the metal nanoparticle into the surrounding medium depends on physical properties of the circumambient material and geometrical properties of metal nanoparticles [17]. The imaginary part of the dielectric constant of a metal nanoparticle represents the key factor for heat distribution calculations around the metal nanoparticle. It is worth noting that Ag nanoparticles under plasmon resonance conditions generate heat about ten times higher than Au nanoparticles out of the resonance.

3.3. Light scattering

There are many technologically feasible ways how to input the metal nanoparticles into a polymer photovoltaic system. Using the solution containing colloidal Ag nanoparticles is one of them[1]. For the nanoparticles with sizes well below the used wavelength, the absorption and scattering of light can be well described using a dipole model [22]. Scattering and absorption cross-sections are given by

$$C_{\text{scat}} = \frac{1}{6\pi}\left(\frac{2\pi}{\lambda}\right)^4 |\alpha|^2, \tag{8}$$

$$C_{\text{abs}} = \frac{2\pi}{\lambda}\,\text{Im}[\alpha], \tag{9}$$

[1] www.bbigold.com

where $$\alpha = 3V\left[\frac{\varepsilon_{\mathrm{NP}}/\varepsilon_0 - 1}{\varepsilon_{\mathrm{NP}}/\varepsilon_0 + 2}\right] \tag{10}$$

is the polarizability of the metal nanoparticle, V is the particle volume, $\varepsilon_{\mathrm{NP}}$ and ε_0 are the dielectric constants of the metal nanoparticle and the surrounding medium, respectively. The dielectric constants $\varepsilon_{\mathrm{NP}}$ and ε_0 are represented in the complex form $\varepsilon_{\mathrm{NP}} = \varepsilon'_{\mathrm{NP}} + \mathrm{i}\varepsilon''_{\mathrm{NP}}$, $\varepsilon_0 = \varepsilon'_0 + \mathrm{i}\varepsilon''_0$, respectively. The polarizability of the nanoparticle is affected by its geometry, as well as by optical properties of the circumambient medium. As the particle size increases, its ability to scatter the light into the surrounding medium increases as well. The ratio of the scattering and the extinction cross-section $C_{\mathrm{scat}}/(C_{\mathrm{scat}} + C_{\mathrm{abs}})$ is called Albedo. For the enhancement of the absorption in an embedding medium, it is desirable that scattering of the metal nanoparticle is higher than its absorption. For illustration, Albedo for Ag and Au nanoparticles with three different diameters is given in table 2. The surrounding medium is P3HT:PCBM$_{(60)}$.

	Albedo (%)
AgØ20	0.7
AgØ100	45.2
AgØ150	73.6
AuØ20	0.1
AuØ100	14.9
AuØ150	37.2

Table 2. Albedo calculated for 20, 100, 150 nm size Ag and Au nanoparticles immersed in P3HT:PCBM$_{(60)}$.

At the surface plasmon resonance, the scattering cross-section can well exceed the geometrical cross-section of the metal nanoparticle. Figures 10-15 show scattering and extinction (scattering plus absorption) cross-sections wavelength dependencies for 20, 40 and 100 nm diameter Ag and Au nanoparticles embedded in ITO, PEDOT:PSS, P3HT:PCBM$_{(60)}$ and vacuum as the reference. The cross-sections, being normalized to the geometrical particle cross section, are calculated using the Mie theory [9], [29]. Dielectric constants are taken from [19]. To characterize the optical constants of P3HT:PCBM$_{(60)}$[2] the spectroscopic ellipsometry has been performed. Optical constants for similar materials have been already measured by other groups [20].

[2] P3HT:PCBM$_{(60)}$ (1:1 by weight), c = 15 mg/mL, dissolved in 1,2-dichlorobenzene.

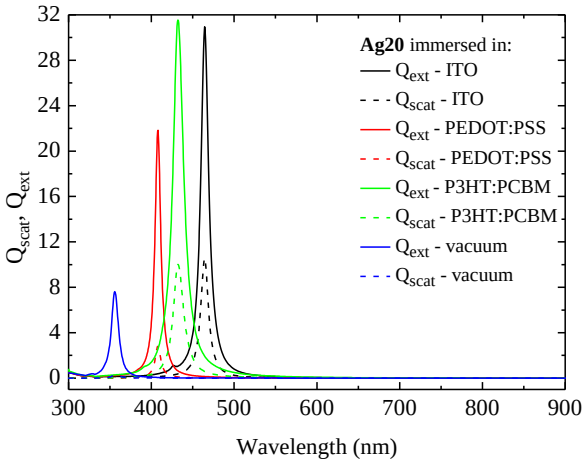

Figure 10. Normalised extinction and scattering cross-sections, calculated for a 20-nm Ag nanoparticle.

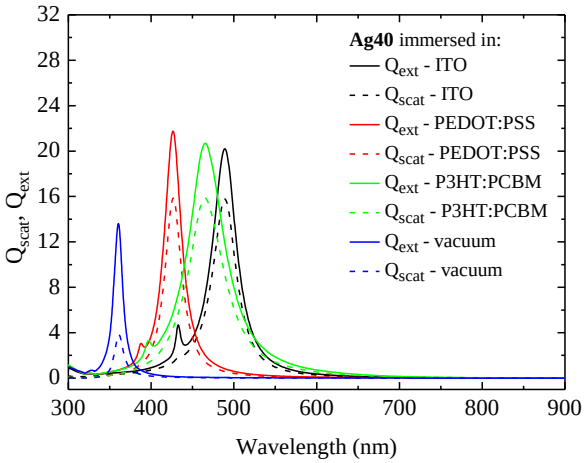

Figure 11. Normalised extinction and scattering cross-sections, calculated for a 40-nm Ag nanoparticle.

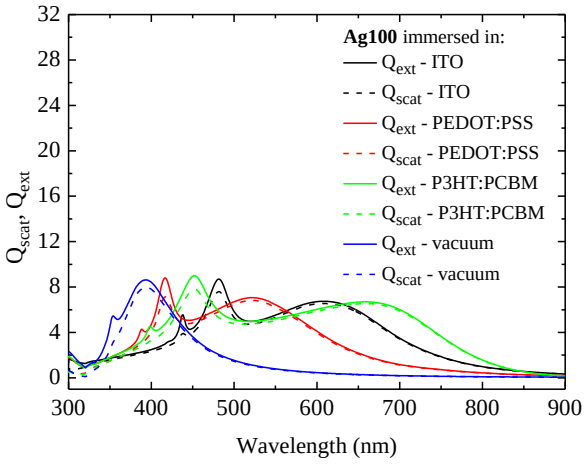

Figure 12. Normalised extinction and scattering cross-sections, calculated for a 100-nm Ag nanoparticle.

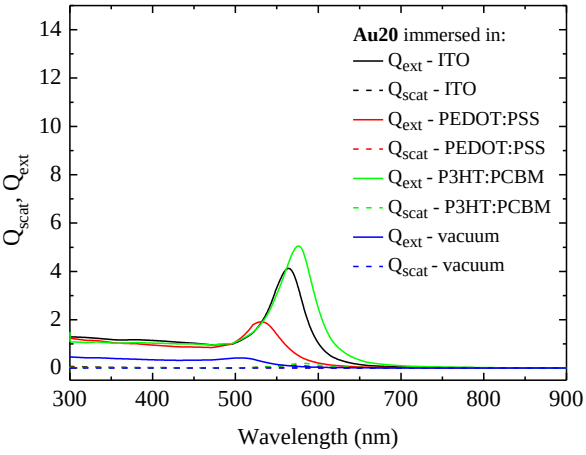

Figure 13. Normalised extinction and scattering cross-sections, calculated for a 20-nm Au nanoparticle.

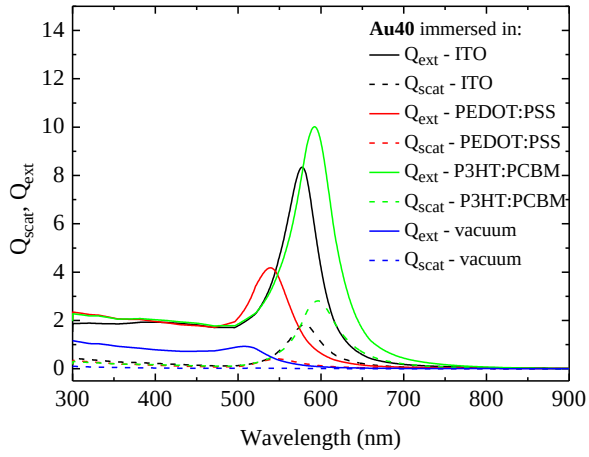

Figure 14. Normalised extinction and scattering cross-sections, calculated for a 40-nm Au nanoparticle.

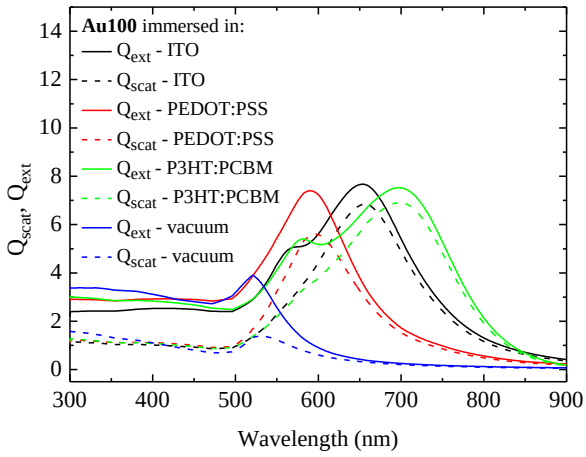

Figure 15. Normalised extinction and scattering cross-sections, calculated for a 100-nm Au nanoparticle.

The concentration of free electrons is higher in Ag nanoparticles than in Au. This results in a blue shift of the surface plasmon resonance compared to Au in case of Ag compared to Au (figures 10-12). Nevertheless, in the infrared wavelength range, dielectric functions of Au and Ag are very similar. In addition, the scattering cross-sections reach higher values for Ag nanoparticles than for Au nanoparticles. Thus, for higher scattering, Ag is the better choice than Au. Further in this work, only Ag nanoparticles will be taken into account. Nevertheless, Ag nanoparticles must be well encapsulated to avoid oxidation effects that are not present for Au. The colloidal nanoparticles consist of a Ag core and a shell which ensures the negative charge of the nanoparticle. The shell is composed of sodium citrate and the medium for Ag nanoparticles is an extra pure distilled water. The encapsulation could significantly affect the light scattering from nanoparticles, resulting in a decrease of the absorption in the surrounding material. Furthermore, the core-shell structure, used in colloidal Ag nanoparticles, can lead to the optical vortexing, which results in the reduction of the photo-generated current [16].

Basically, the higher index of the embedding medium leads to the red-shift of the surface plasmon resonance. Also, the light is scattered preferentially into a dielectric with larger permittivity. The evanescent plasmon field extends more than 100 nm into the polymer whereas it only extends a few nanometers into the metal. As the result, the optical path length is effectively increased in the dielectric medium. The shift of the plasmon resonance and the contribution of higher order multipoles need to be considered for all solar cell geometries. In particular, for arrangements with metal nanoparticles within the active layer of solar cells. For such a configuration, it is also required to avoid bimolecular recombinations of electron-hole pairs at the metal-semiconductor interface. However, applying metal nanoparticles at the front side of solar cells seems to be a better option [21]. Otherwise, a reduced driving field close to the substrate causes the decrease in the relative scattering cross-section. This driving field is caused by the interference of the incident and reflected radiation [22].

4. ELECTROMAGNETIC SIMULATIONS

It is rather complicated to simulate plasmonic effects in organic multilayer structures such as solar cells based on P3HT:PCBM$_{(60)}$. To perform these simulations, it is necesarry to know optical constants of each layer being present in that system. There are many powerful electromagnetic simulation methods able to calculate plasmonic tasks, including local surface plasmon polaritons and their resonances. Some of them are based on the surface integral equation solution, volume integral equations and boundary element methods [9]. Here, we use the software Lumerical (Lumerical Solutions, Inc.) which uses a Finite-Difference Time-Domain (FDTD) method.

4.1. Finite-Difference Time-Domain method

The Finite-Difference Time-Domain method (FDTD) is a simulation technique frequently used in electromagnetism. From the FDTD methods, we obtain the frequency spectra by exploiting Fourier transforms at the full range of wavelengths. The FDTD method is a grid-based differential numerical method. First, the electric intensity *E* is solved in the differential volume d*V* and the magnetic induction *H* is solved consequently. We can easily define materials by the real and imaginary parts of optical constants. Maxwell's equations which are solved by this method are of the form

$$D(\omega) = \varepsilon_0 \varepsilon_r(\omega) E(\omega), \tag{11}$$

$$\frac{\partial D}{\partial t} = \nabla \times H, \tag{12}$$

$$\frac{\partial H}{\partial t} = -\frac{1}{\mu_0} \nabla \times E, \tag{13}$$

where $\varepsilon_r(\omega) \in \Im m$ and $\varepsilon_r(\omega) = n^2(\omega)$.

There are six field components $E_x, E_y, E_z, H_x, H_y, H_z$ in three dimensional space to be solved. Boundary conditions have the natural meaning in theory. Nevertheless, they can be introduced differently in the simulation process. There is a set of boundary conditions available in FDTD softwares:

- absorbing boundary conditions allowing the field to escape from the computational volume. The field is absorbed by the boundary and it can not be reflected back to the computational volume. As the absorbing boundary conditions are realized by many layers, we have to pay attention to their setup.

- Perfectly Matched Layers (PML) represent the frequently used absorbing boundaries.

- periodic boundary conditions. In this case, the unit cell is defined. We acquire the field of an infinite number of cells, even though the software computes only one cell.

- metallic boundary conditions providing perfect reflection at a boundary. The energy is kept constant in the computational volume.

- symmetric boundary conditions referring a mirror symmetry for the electric field and an anti-mirror symmetry for the magnetic field.

- antisymmetric boundary conditions involving an anti-mirror symmetry of the electric field and a mirror symmetry for the magnetic field.

While the calculation is running in the whole space terminated by boundaries, the software saves the calculated field only in a pre-selected space which is called the monitor. The simulation is finished when the monitor is achieved. The monitor can be defined by diverse geometrical shapes. The components of the calculated electromagnetic field are saved together with the components of the Poynting vector. If discrete optical constants for a required range of wavelengths are availabe, the software will fit them.

Geometrical setup of objects used in FDTD simulations as a glass substrate, ITO, PEDOT:PSS, P3HT:$PCBM_{(60)}$, LiF and Al is illustrated in figure 16.

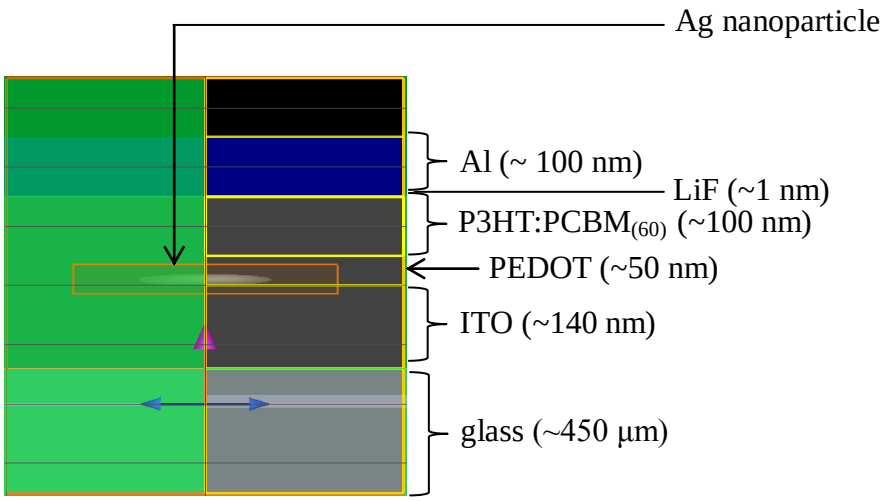

Figure 16. Setup of objects used in FDTD simulations. As there are symmetrical elements in our system and the FDTD methods work with PML boundary conditions, it is possible to perform simulations only for one half of the system (black area at the right side of the picture). It saves the simulation time and reduces memory requirements significantly.

4.2. Results of simulations

In this section, the issue of the increasing absorption of the photovoltaic system based on P3HT:PCBM$_{(60)}$ is discussed. The absorption originating from surface plasmon resonances has been confirmed by experimental reflection studies and theoretical modeling (FDTD simulations). To overcome absorption limits of the photoactive layer, different geometrical arrangements of Ag nanoparticles inside the bulk heterojunction photovoltaic system is reported. It will be shown in agreement with [13] that the surface plasmon absorption bands are dependent on the size, shape, density, and local dielectric environment of the nanoparticle. The simulation has been performed for 16, 20 and 40 nm Ag nanoparticles. For each diameter, only the position and the distance between the nanoparticles in the polymer photovoltaic system change have been changed. To perform simulations, it was necessary to know all optical constants of materials used in the simulation. Figures 17-25 illustrate the refractive index and extinction coefficient for all materials being used in this work.

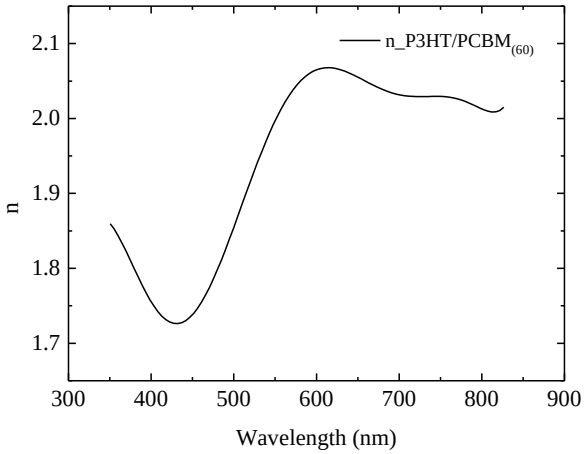

Figure 17. Refractive index for P3HT: PCBM$_{(60)}$.

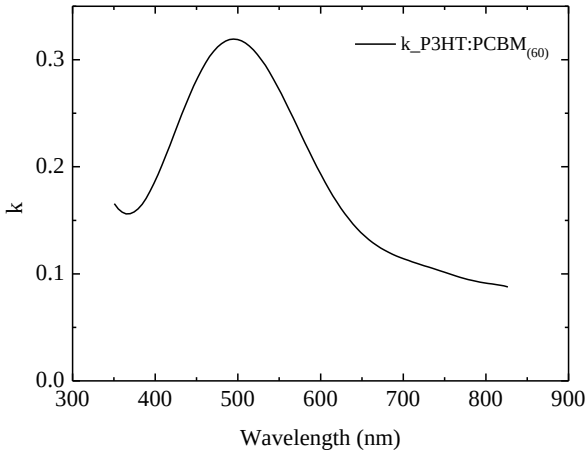

Figure 18. Extinction coefficient for P3HT:PCBM$_{(60)}$.

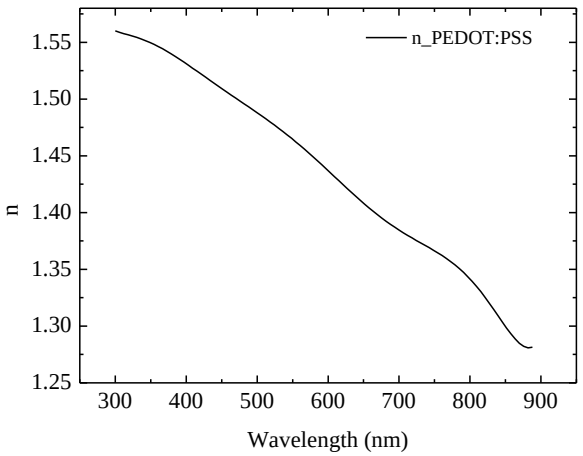

Figure 19. Refractive index for PEDOT:PSS.

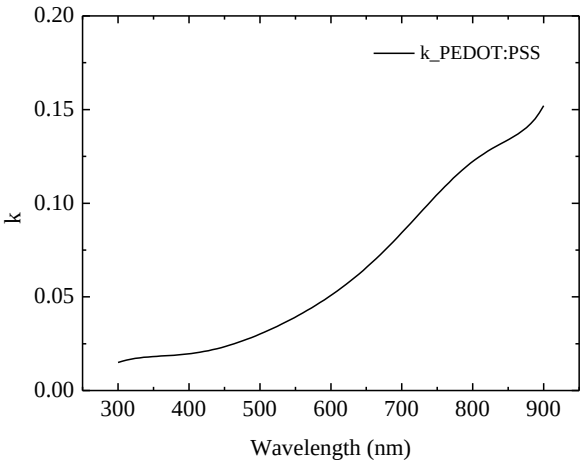

Figure 20. Extinction coefficient for PEDOT:PSS.

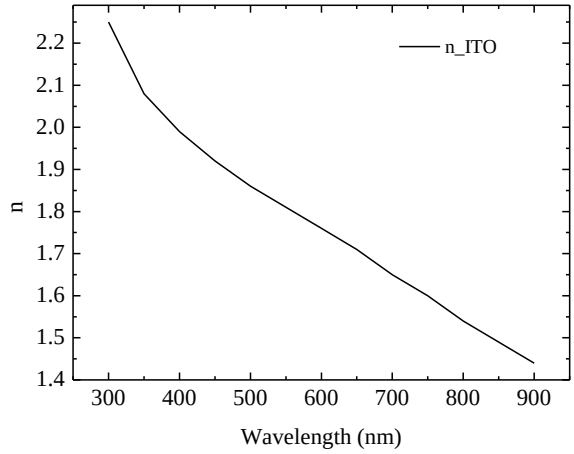

Figure 21. Refractive index for ITO.

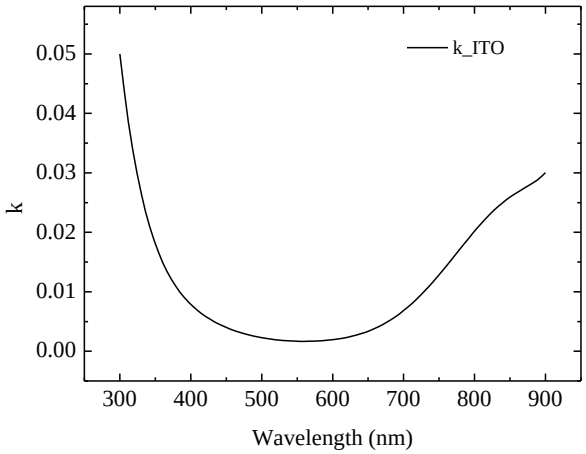

Figure 22. Extinction coefficient for ITO.

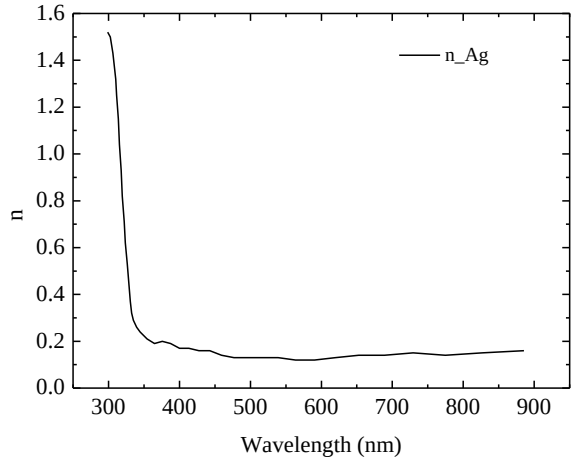

Figure 23. Refractive index for Ag.

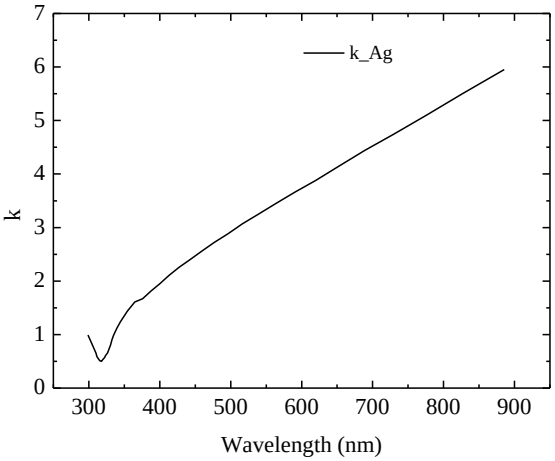

Figure 24. Extinction coefficient for Ag.

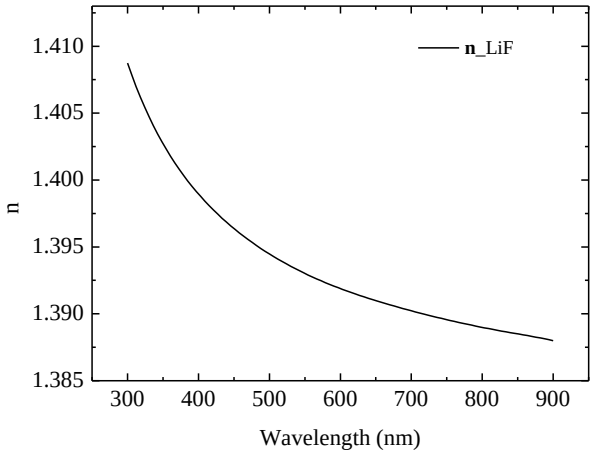

Figure 25. Refractive index for LiF.

Figures 17-25 show optical constants of all important materials used in this work. To obtain optical constants for P3HT:PCBM$_{(60)}$ and PEDOT:PSS, the spectroscopic ellipsometry has been performed. Optical constants for ITO, LiF and Ag have been taken from [6]. In our experiments, P3HT:PCBM$_{(60)}$ (1:1) was used with concentration about 15 mg/mL (solvent 1,2-dichlorobenzene). The values of extinction coefficients for LiF are too low to be presented [6].

The part below is devided into three parts where the influence of Ag nanoparticles for their different locations in the system are studied. In each part, the location of Ag nanoparticles in the system is kept constant and only their geometrical arrangement is changed. Especially, the absorption and electric intensity for each geometrical arrangement is discussed. The enhancement of the absorption in the photoactive layer ($P3HT:PCBM_{(60)}$) is the key factor which can lead to an increase in power conversion efficiency of the studied polymer photovoltaic system. In these simulations Ag nanoparticles are supposed to be homogeneously distributed in the perfect monolayer and without creating clusters. The fabrication and the measurement of such modified devices is discussed in the next chapter.

4.2.1. Ag nanoparticles positionned on the PEDOT:PSS - ITO interface

The schematic layout of this arrangement is shown in figure 26. In all cases, the substrate is illuminated from the bottem side, as shown by the propagation vector $\vec{k}$.

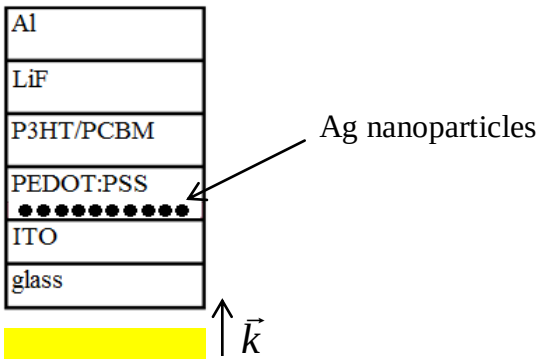

Figure 26. Schematic layout of Ag nanoparticles positionned at the PEDOT:PSS - ITO interface.

Figures 27-32 show the absorption of electromagnetic energy in PEDOT:PSS and in the photoactive layer. In addition, the absorption in $P3HT:PCBM_{(60)}$ without Ag nanoparticles is plotted as the reference. If the $P3HT:PCBM_{(60)}$ absorption curve exceeds the reference one, then the photoactive layer of a device modified with Ag nanoparticles exhibits a higher absorption compared to the reference one. This absorption enhancement can be seen for the arrangement with 20-nm Ag nanoparticles with the spacing about 40 nm (figure 30). In this case, the absorption curve of the photactive layer well exceeds the reference it the wavelength range from 470 to 900 nm.

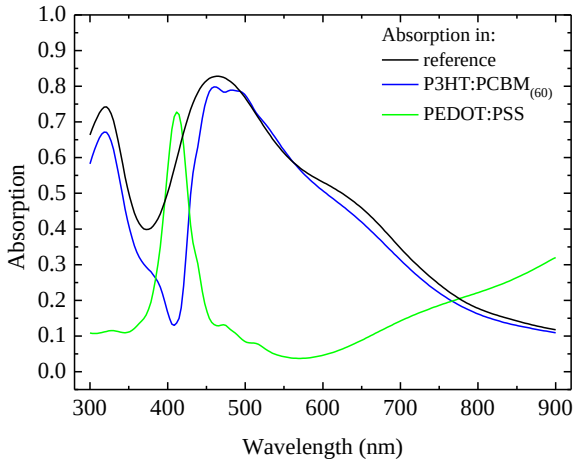

Figure 27. Electromagnetic wave absorption spectra (Ag, Ø16 nm, spacing 16 nm).

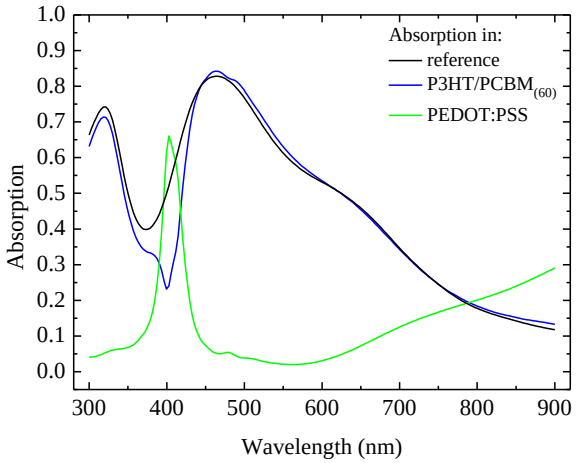

Figure 28. Electromagnetic wave absorption spectra (Ag, Ø16 nm, spacing 32 nm).

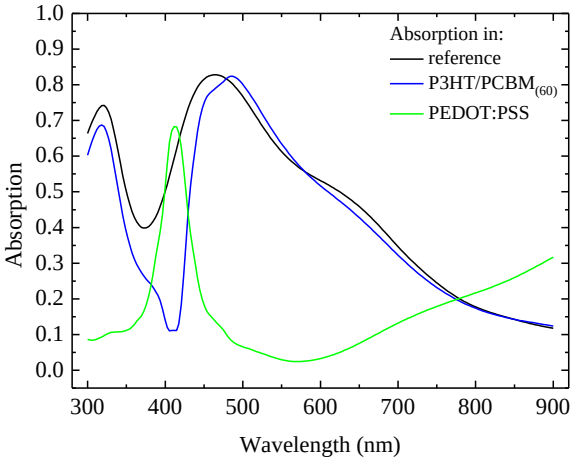

Figure 29. Electromagnetic wave absorption spectra (Ag, Ø20 nm, spacing 20 nm).

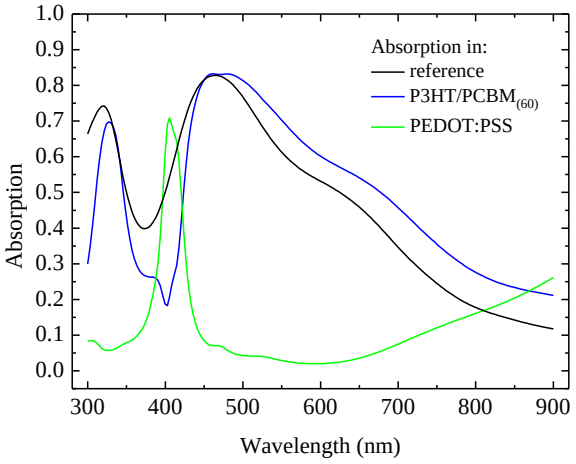

Figure 30. Electromagnetic wave absorption spectra (Ag, Ø20 nm, spacing 40 nm).

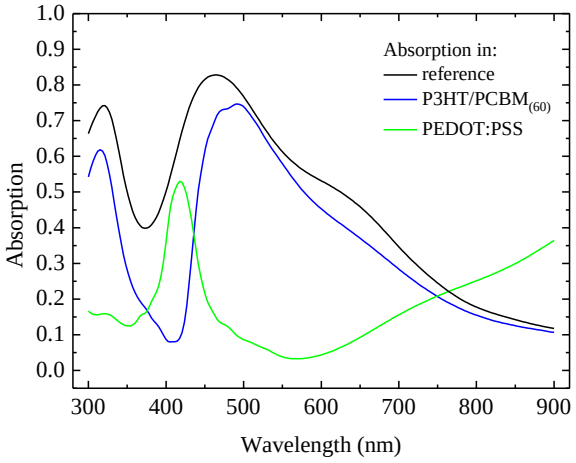

Figure 31. Electromagnetic wave absorption spectra (Ag, Ø40 nm, spacing 40 nm).

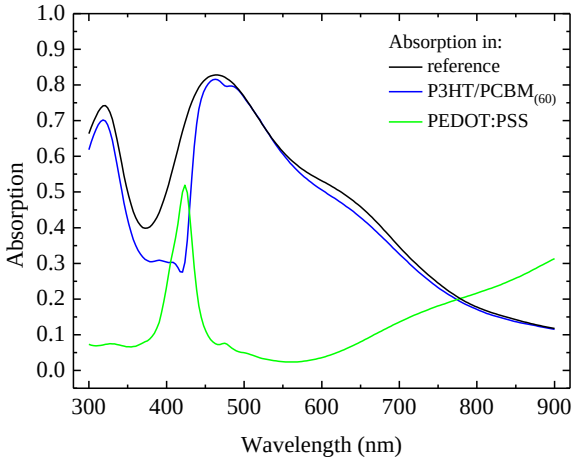

Figure 32. Electromagnetic wave absorption spectra (Ag, Ø40 nm, spacing 100 nm).

The increased absorption in the photoactive layer (illustrated in figure 30 and partially in figure 29) is the result of the significantly enhanced local electromagnetic field in the vicinity of Ag nanoparticles. This effect also leads toan increase of the exciton generation [17]. Figure 33 illustrates thespectral dependence of the square of the magnitude of electric intensity $|E|^2$ around the nanoparticle. As a reference, the curve for the sample without without Ag nanoparticles is shown.

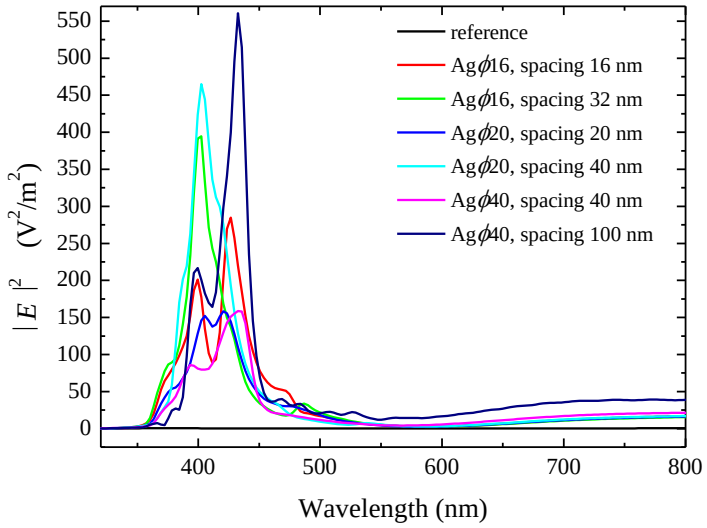

Figure 33. Square of the magnitude of electric intensity in the vicinity of Ag nanoparticle located at the PEDOT:PSS - ITO interface as a function of wavelength.

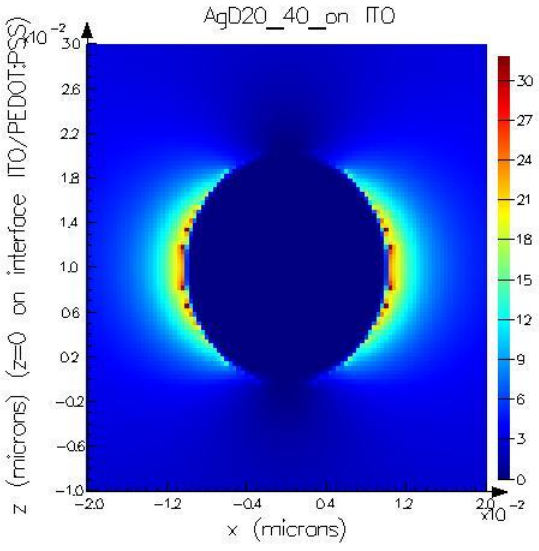

Figure 34. Electric field distribution of $|E|^2$ (V^2/m^2) in the vicinity of a 20-nm Ag nanoparticle with a 40 nm separation located on the layer ITO.

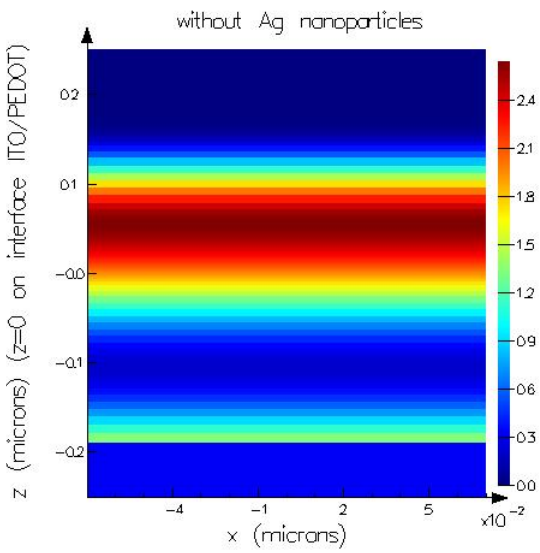

Figure 35. Electric field distribution of $|E|^2$ (V^2/m^2) of the sample without nanoparticles.

Figure 34 shows $|E|^2$ in the vicinity of 20 nm diameter Ag nanoparticle with the spacing about about 40 nm. Units presented at the bottom and on the left side are microns. The colored scale on the right side expresses the relative enhancement of $|E|^2$ around the nanoparticle. These values are normalised to $|E|^2$ of the reference system without nanoparticles. Here,the blue color means zero enhancement and the red color means the multiple of the enhancement compared to the zero enhancement.

4.2.2 Ag nanoparticles positionned in P3HT:PCBM$_{(60)}$

With regards to simulations, the immersion of Ag nanoparticles directly into the photoactive layer offers an ideal solution how to effectively enhance the light absorption in this layer. On the other hand, this way presents a lot of complications dealing with the preparation of the P3HT:PCBM$_{(60)}$ blend being modified with Ag nanoparticles. The schematic layout of this arrangement is shown in figure 36 where the substrate is illuminated from the lower side, as shown by the propagation vector $\vec{k}$.

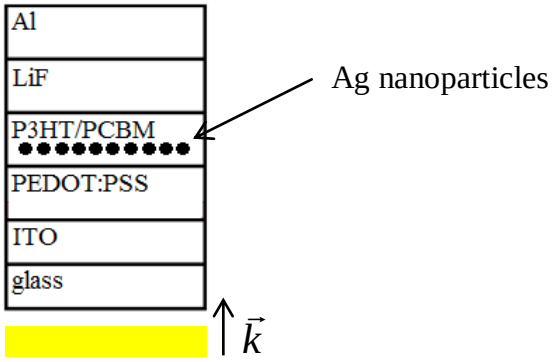

Figure 36. Schematic layout of Ag nanoparticles positionned in the photoactive layer.

For this configuration, the absorption of electromagnetic energy in the photoactive layer and the PEDOT:PSS layer is shown in figures 37-42. The absorption in the P3HT:PCBM$_{(60)}$ layer without Ag nanoparticles is plotted as a reference (solid black line). For this geometrical arrangement, it is easily seen that all P3HT:PCBM$_{(60)}$ absorption curves of Ag modified devices exceed the reference curve. For all these configurations there is a significant enhancement of the absorption compared to the arrangement with Ag nanoparticles placed on the PEDOT:PSS - ITO interface. This increase in absorption occurs nearly for the whole range of wavelengths. In addition, for all these curves, a small peak around 400 nm of wavelengths occurs. This extra peak results from resonance effects in Ag that contribute to the enhancement of electromagnetic wave absorption in the photoactive layer. As this peak is more pronounced for the system with smaller inter-particle distances, it may be connected with resonance coupling between the nanoparticles.

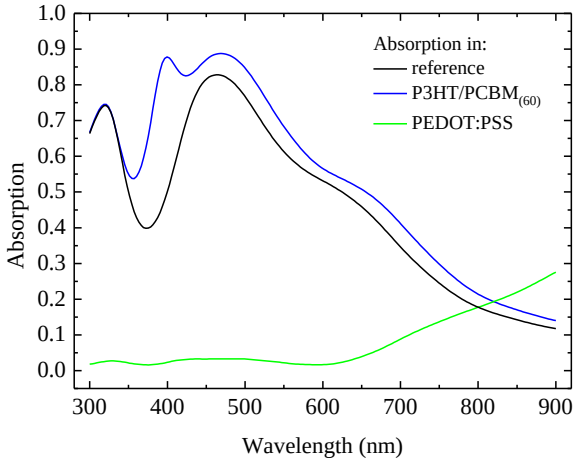

Figure 37. Electromagnetic wave absorption spectra (Ag, Ø16 nm, spacing 16 nm).

.

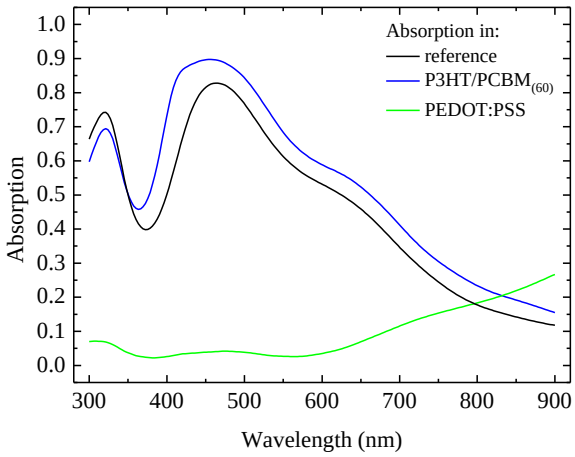

Figure 38. Electromagnetic wave absorption spectra (Ag, Ø16 nm, spacing 32 nm).

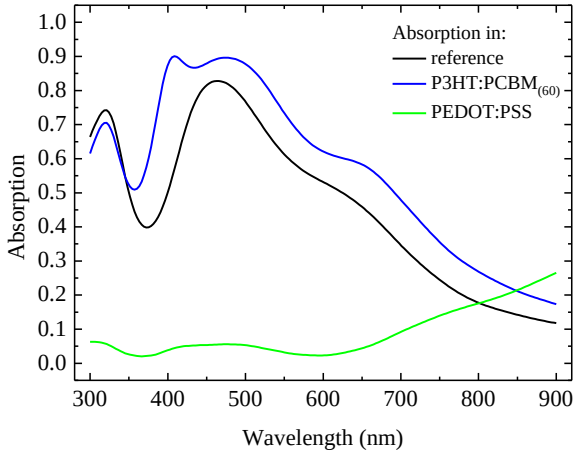

Figure 39. Electromagnetic wave absorption spectra (Ag, Ø20 nm, spacing 20 nm).

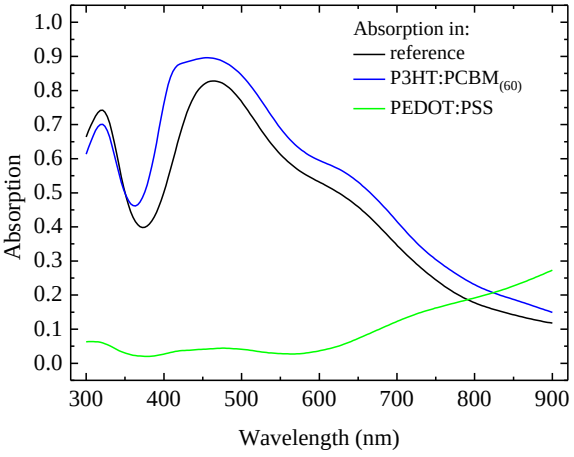

Figure 40. Electromagnetic wave absorption spectra (Ag, Ø20 nm, spacing 40 nm).

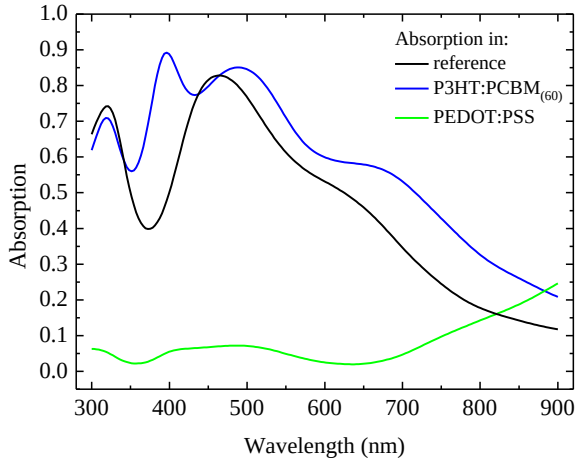

Figure 41. Electromagnetic wave absorption spectra (Ag, Ø40 nm, spacing 40 nm).

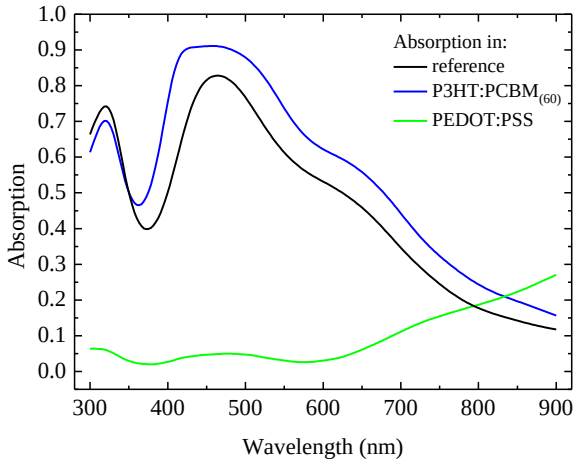

Figure 42. Electromagnetic wave absorption spectra (Ag, Ø40 nm, spacing 100 nm).

However, although the increase of the exciton creation in the active layer is essential, in the end, it is necessaery to take the bimolecular recombinations between the separated charges into account [3]. Figure 43 illustrates the spectral dependence of the square of the magnitude of electric intensity in the vicinity of Ag nanoparticles. As a reference, the system without nanoparticles is shown.

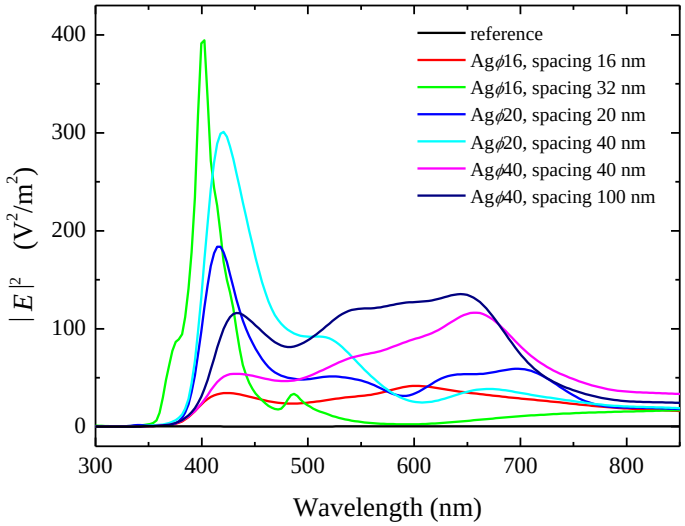

Figure 43. $|E|^2$ in the vicinity of Ag nanoparticles located in the active layer as a function of wavelength. For 16-nm Ag nanoparticle, the maximum value is nearly 400x higher compared to the reference.

These simulations require the knowledge in the electromagnetic field in surrounding of Ag nanoparticle. The spatial distribution of $|E|^2$ around a Ag nanoparticle is shown in figures 44 and 45. Here, the configuration without nanoparticles is used as the reference.

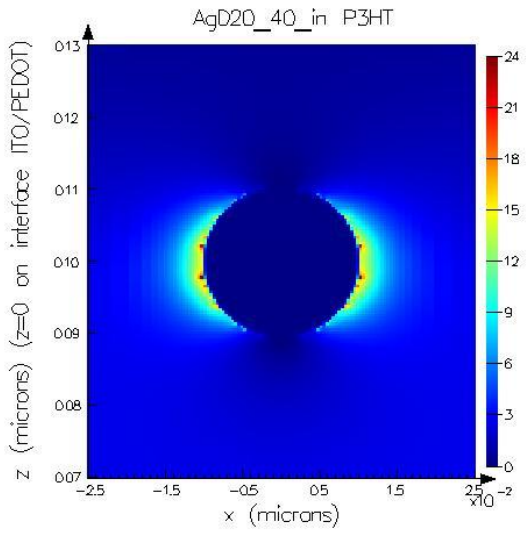

Figure 44. Electric field distribution of $|E|^2$ (V^2/m^2) in the vicinity of 20-nm Ag nanoparticle with a 40 nm separation immersed in the active layer.

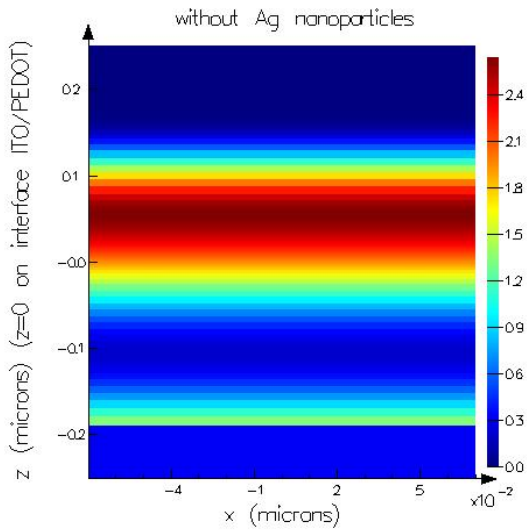

Figure 45. Electric field distribution of $|E|^2$ (V^2/m^2) of the sample without nanoparticles.

For the geometrical arrangement illustrated in figure 44, the distance between 20-nm Ag nanoparticles was about 40 nm. The maximal increase of the square electric intensity magnitude is observed for the P3HT:PCBM$_{(60)}$ layer where excitons are created.

4.2.3. Ag nanoparticles positionned on the PEDOT:PSS - ITO interface and in P3HT:PCBM$_{(60)}$

This arrangement represents a combination of the two previous methods. Here, simulations have proved a significant enhancement of the absorption in PEDOT:PSS and in P3HT:PCBM$_{(60)}$ layer. Nevertheless, the numerical calculations show that the "shade" of electric intensity around Ag nanoparticles in the lower layer affects the electric intensity of Ag nanoparticles in the upper layer. Since, the device is illuminated from the bottom side, Ag nanoparticles in the lower layer provides the higher enhancement in electric intensity than the upper nanoparticles. From the geometrical arrangement it is clear that the lower layer (PEDOT:PSS) absorbs more light than the upper one (P3HT:PCBM$_{(60)}$). However, their difference in $|E|^2$ is not so significant at first sight (figure 54). As shown at the previous structures, this configuration presents a lot of complications concerning the fabrication. The schematic layout of such an arrangement is shown in figure 46. The substrate is illuminated from the bottom side, as shown by the propagation vector $\vec{k}$.

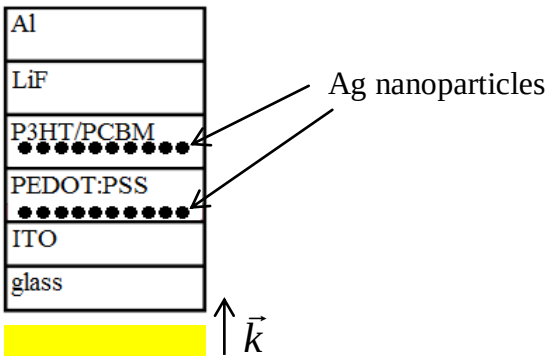

Figure 46. Schematic layout of Ag nanoparticles positionned both at the PEDOT:PSS - ITO interface and in the P3HT:PCBM$_{(60)}$ layer.

Figures 47-52 illustrate electromagnetic energy absorption in the photoactive layer induced by Ag nanoparticles situated not only on the ITO layer but also in the blend P3HT:PCBM$_{(60)}$. As compared with the previous arrangement where nanoparticles are embedded directly into the photoactive layer, the enhancement of the absorption is more significant for the wavelengths above 500 nm. For the wavelengths below 500 nm, the absorption in P3HT:PCBM$_{(60)}$ is rather smaller. With respect to the absorption in PEDOT:PSS, it is possible to clearly see the peak at wavelengths around 430 nm. This plasmon-resonance related peak is not present for the arrangement with Ag nanoparticles immersed only in P3HT: PCBM$_{(60)}$.

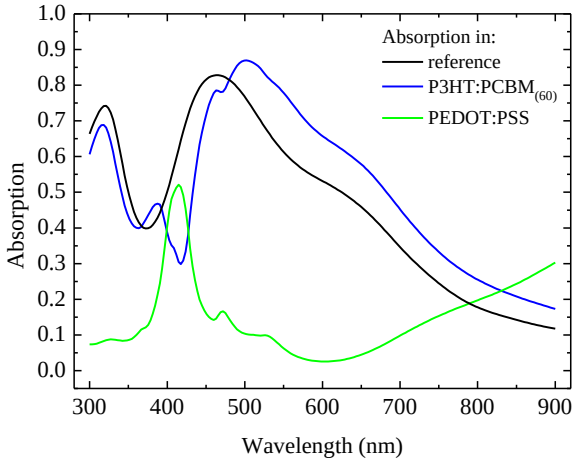

Figure 47. Electromagnetic wave absorption spectra (Ag, Ø16 nm, spacing 16 nm).

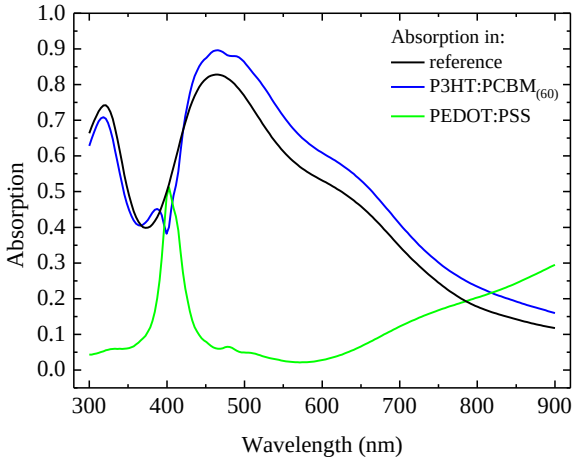

Figure 48. Electromagnetic wave absorption spectra (Ag, Ø16 nm, spacing 32 nm).

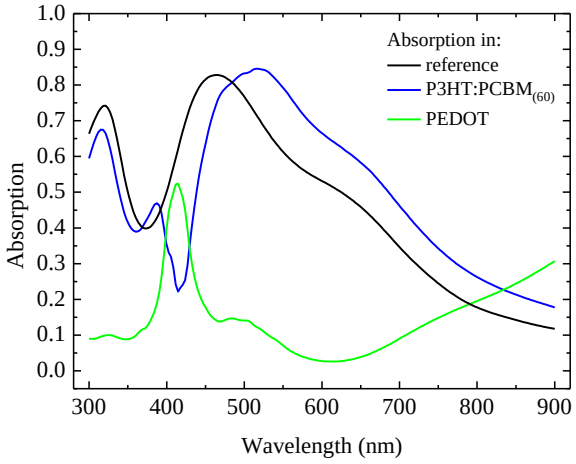

Figure 49. Electromagnetic wave absorption spectra (Ag, Ø20 nm, spacing 20 nm).

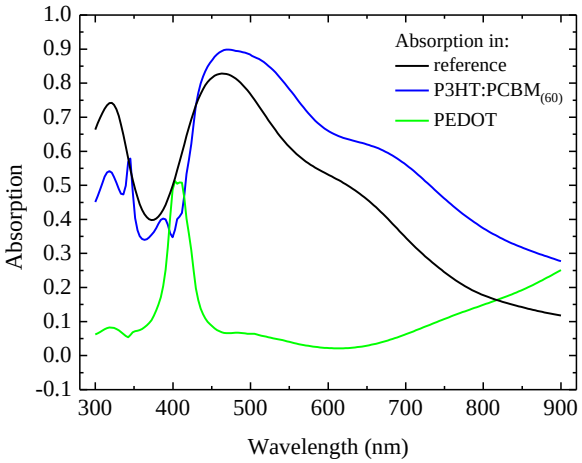

Figure 50. Electromagnetic wave absorption spectra (Ag, Ø20 nm, spacing 40 nm).

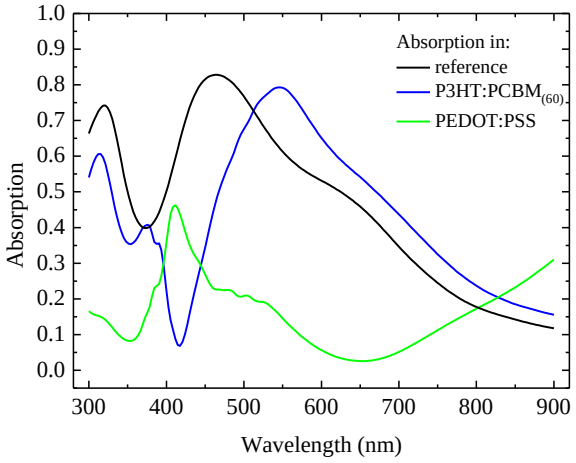

Figure 51. Electromagnetic wave absorption spectra (Ag, Ø40 nm, spacing 40 nm).

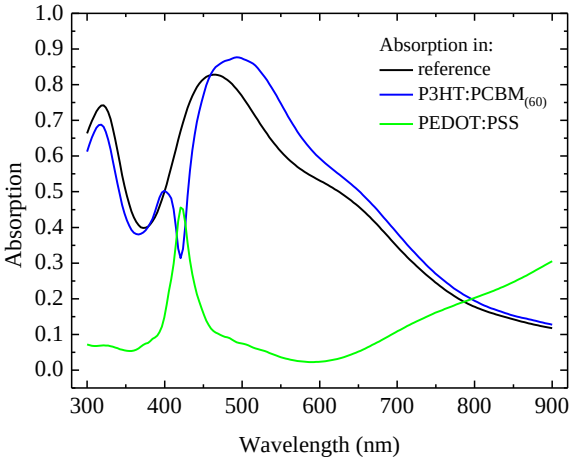

Figure 52. Electromagnetic wave absorption spectra (Ag, Ø40 nm, spacing 100 nm).

Figure 53 illustrates the spectral dependence of the square of the magnitude of electric intensity around Ag nanoparticles. As a reference the dependence for the reference sample without Ag nanoparticles is shown.

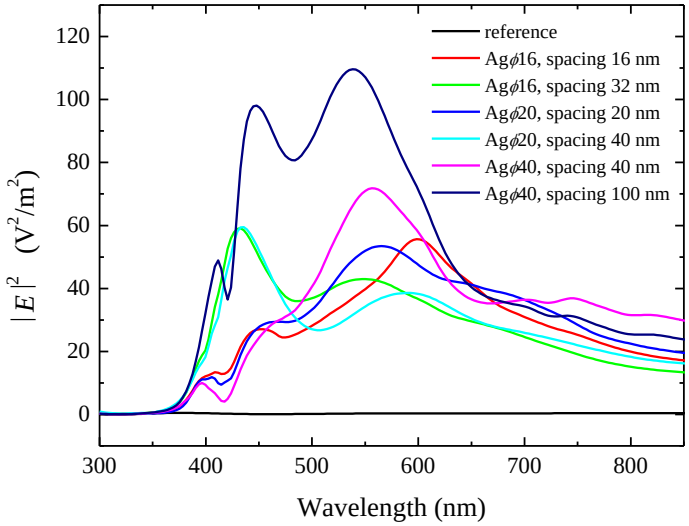

Figure 53. $|E|^2$ in the vicinity of Ag nanoparticle located both in the active layer and PEDOT:PSS as a function of wavelength. For a 40-nm Ag nanoparticle, the maximum value is more than 100x higher compared to the reference.

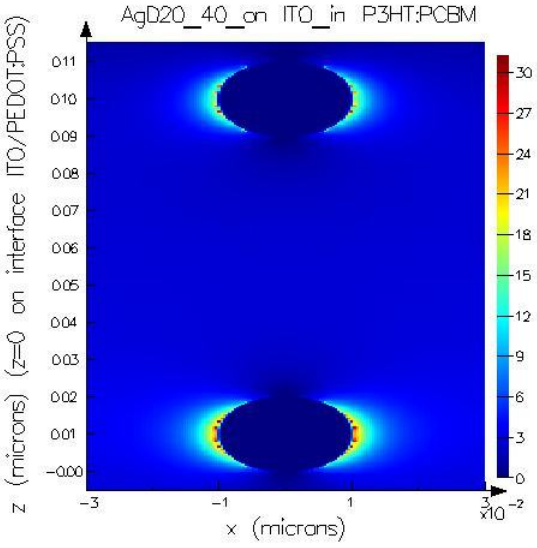

Figure 54. Electric field distribution of $|E|^2$ (V²/m²) in the vicinity of a 20-nm Ag nanoparticle with a 40 nm separation located in the active layer and on the layer ITO.

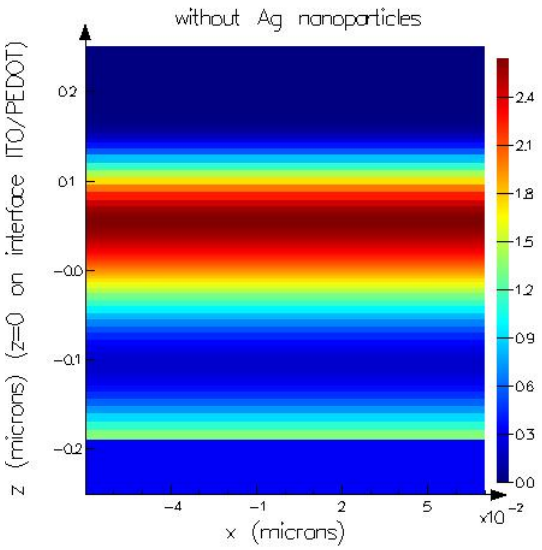

Figure 55. Electric field distribution of $|E|^2$ (V²/m²) of the sample without nanoparticles.

From figure 54 it is evident that the enhancement in $|E|^2$ is more significant around the lower Ag nanoparticle. To eliminate the "shade" of the electric intensity created by the lower sphere, a modified configuration where Ag nanoparticles do not overlap was proposed (figure 56). However, this configuration does not exhibit any improvement in $|E|^2$ compared to the arrangement displayed in figure 54. Even more, the absorption caused by this arrangement has significantly dropped below the absorption of the reference sample without Ag nanoparticles (figure 57).

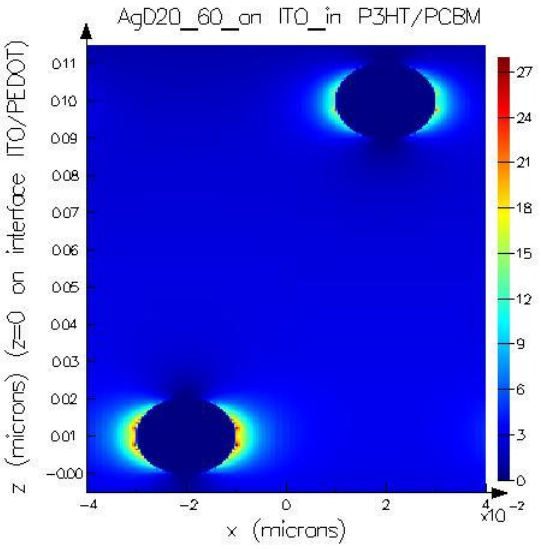

Figure 56. Electric field distribution of $|E|^2$ [V^2/m^2] in the vicinity of a 20-nm Ag nanoparticle with a 60 nm separation located in the active layer and on the layer ITO.

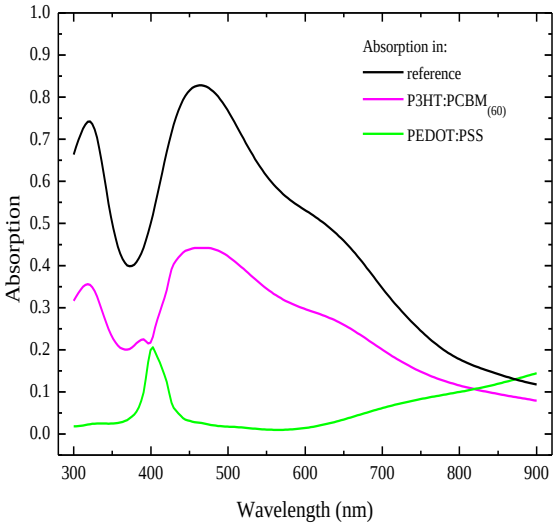

Figure 57. Electromagnetic wave absorption spectra (Ag, Ø20 nm, spacing 60 nm).

5. EXPERIMENTAL SECTION

In this chapter, the device fabrication and measurement techniques will be presented. The first part of this section is devoted to the preparation of P3HT:$PCBM_{(60)}$ based devices. Therefore, the fabrication of reference samples and samples modified with Ag nanoparticles is described in detail and the technique used to the measurements is discussed in the second part. The results achieved from this experiment will be shown during this chapter.

5.1. Device fabrication

In this experimental part, four series consisting of four samples, i.e. 16 samples in total were fabricated. Considering the numerical simulations, discussed in the previous chapter, the precise configuration and dimensions of the prepared devices cannot be achieved. There are only a few methods how to incorporate the Ag nanoparticles into the photovoltaic system based on P3HT:$PCBM_{(60)}$. For example, a pulse-current electrodeposition (PCED) can be applied [13], which is the method that controls the density and size of metal nanoparticles. In this method, metal ions are supplied from the bulk solution to the substrate during the time when the current supply is switched-off. Thus, the particle size and density can be tuned via controlling the current density during the switched-off and switched-on time period (figure 58).

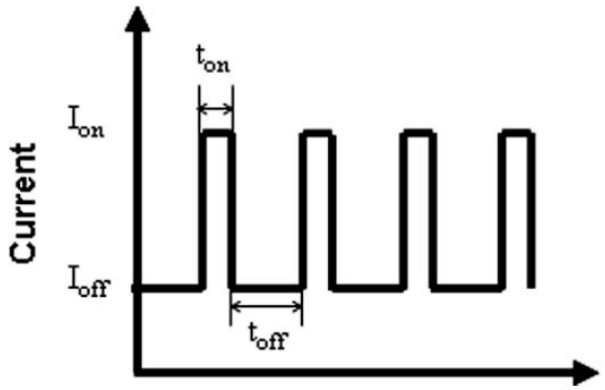

Figure 58. Principle of the pulse-current electrodeposition [13].

Another way how to insert Ag nanoparticles into the system is the organic vapor-phase deposition (OPVD). By this method, organic molecules are uniformly depositied on a cold substrate from a hot inert carrier gas (figure 59).

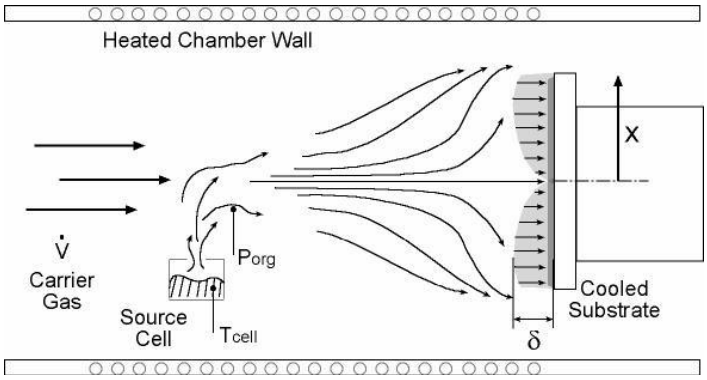

Figure 59. Scheme of the organic vapor-phase deposition process (OPVD) [23].

However, these two methods are complex and need quite a special equipment. In the following parts, three other methods, how to put Ag nanoparticles inside individual layers will be discussed.

5.1.1. Fabrication of reference samples

Before fabrication of samples modified with Ag nanoparticles, a few substrates serving as the reference ones, were prepared.

In principle, the building of these devices can be described in six steps:

- Cleaning the substrates
- Fast drying with inert gas
- Inserting the substrates into a UV ozone oven
- Preparing solutions
- Spin coating of the solutions
- Evaporation of LiF/Al electrodes on substrates

Before the processing, it is necessary to clean all the substrates in a soap and then put them into an ultrasound bath filled with aceton. This is made in order to clean substrates from fats. Afterwards, the substrates are fast dried by an inert gas (N_2) and put into a UV ozone oven. In the UV ozone oven, organic residues are removed. While keeping samples in the UV ozone oven, it is desirable to prepare required solutions. Here, it is used a solution of P3HT as the electron donor and $PCBM_{(60)}$, due to its high hole mobility as the electron acceptor. The concentration of P3HT:$PCBM_{(60)}$ (1:1 by weight) is 15 mg/mL and 1,2-dichlorobenzene is chosen as the solvent. The individual steps of the whole process are schematically illustrated in a simple way in figure 60.

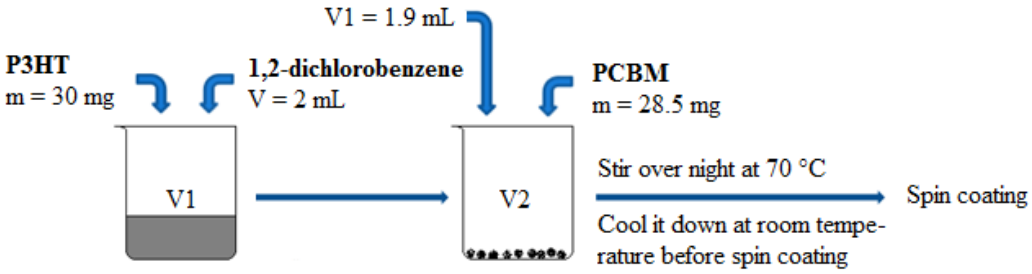

Figure 60. Preparation of P3HT/PCBM$_{(60)}$ (1:1 by weight), *c* = 15 mg/mL. During the transfer from *V1* to *V2*, 5% losses are taken into account.

Another step is the spin-coating of PEDOT:PSS and P3HT:PCBM$_{(60)}$ on glass substrates. PEDOT:PSS is the conducting polymer whose function is to reduce the roughness of ITO layer and mainly to collect positive charges (holes). Before spin-coating, the solution of PEDOT:PSS must be filtred to avoid the residual impurities. The big advantage of spin-coating is the uniform spreading of the solution on a subsrate. The principle of the spin-coating method is illustrated in figure 61. The layer thickness (*d*) as a function of the spinning speed (expressed in revolutions per minute) is given in figure 62.

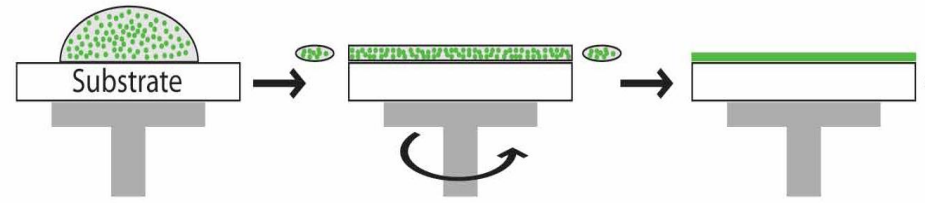

Figure 61. Schematic of the spin-coating method [24].

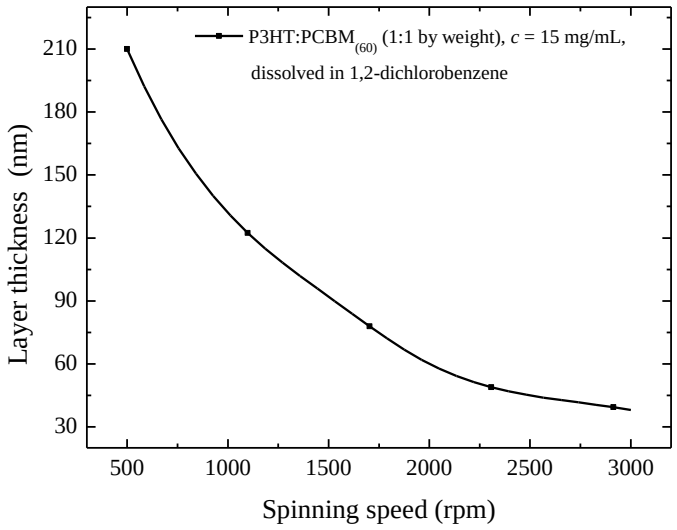

Figure 62. Layer thickness as a function of the spinning speed. (The layer of P3HT:PCBM$_{(60)}$ (1:1), *c* = 15 mg/mL, dissolved in 1,2-dichlorobenzene).

The final thickness of a coated layer is proportional to $\omega^{-1/2}$ as can be seen from equation 14 [24]. The spin-coating method has been carried out in the air atmosphere, at room temperature and under the normal pressure (1013 hPa). Before the spin-coating of the photoactive layer it is necessary to deposit the filtered PEDOT:PSS. This is usually applied at 3000 rpm for one minute. Under these conditions, the layer PEDOT:PSS of approximately 50 nm is created.

$$h_f \propto \left(\frac{\eta_0}{\rho\omega}\right)^{-1/2}\left(1-x_1^0\right), \tag{14}$$

where η_0 is the initial solution viscosity, ρ is the solution density, ω is the spinnig speed and x_1^0 is the initial solvent mass fraction in the spin-coated solution. For all the samples, P3HT:PCBM$_{(60)}$ has been spin coated at 2500 rpm for 200 seconds.

The next step is the evaporation of lithium fluoride (LiF) and aluminium electrodes (Al). LiF (~1 nm) and Al (~100 nm) are deposited consecutively in a vacuum chamber (~ 10^{-7} Pa) located in a glove box. The role of LiF is to improve the adhesion and transport of electrons between the active layer and Al electrode. The deposition is controlled automatically by an appropriate software. Even if the substrates are placed in the glove box, they are sensitive to degradation. Thus, the processing time and the measurement of prepared samples should be performed as fast as possible. After finishing the fabrication process it is required to anneal all the samples. This is made in order to improve not only their morphological, optical and physical properties, but especially to improve the charge carrier mobility in the photoactive layer [8]. In our case, all samples have been annealed at 110 °C for 30 minutes.

5.1.2. Fabrication of samples modified with Ag nanoparticles – Spin-coating method

The spin-coating method is a powerful method intended for the preparation of very thin films in the liquid form. However, this method has some limits while applying colloidal Ag nanoparticles. For this kind of experiments, 20, 40 and 80 nm diameter colloidal Ag nanoparticles have been available[3]. These colloidal metal nanoparticles consist of a Ag core and the shell based on sodium citrate ($Na_3C_6H_5O_7$, figure 63). The surrounding medium is the highly purified water. The shell of sodium citrate provides the negative charge to nanoparticles, allowing them to repel each other and thus to prevent their aggregation [16]. The concentration of the solution with colloidal Ag nanoparticles is 7.10^{10} particles in 1 mL. In our case, the P3HT:PCBM$_{(60)}$ layer thickness is only about 60 nm. Hence, only 20-nm Ag nanoparticles are used to avoid some unfavorable consequences as the P3HT:PCBM$_{(60)}$ layer is very sensitive even to the slightes structural and morphological changes. Figure 64 illustrates the absorbance spectra for 20, 40, 60 and 80-nm Ag nanoparticles surrounded by the air.

[3] www.bbigold.com

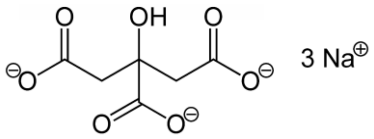

Figure 63. Molecular structure of sodium citrate - $Na_3C_6H_5O_7$.

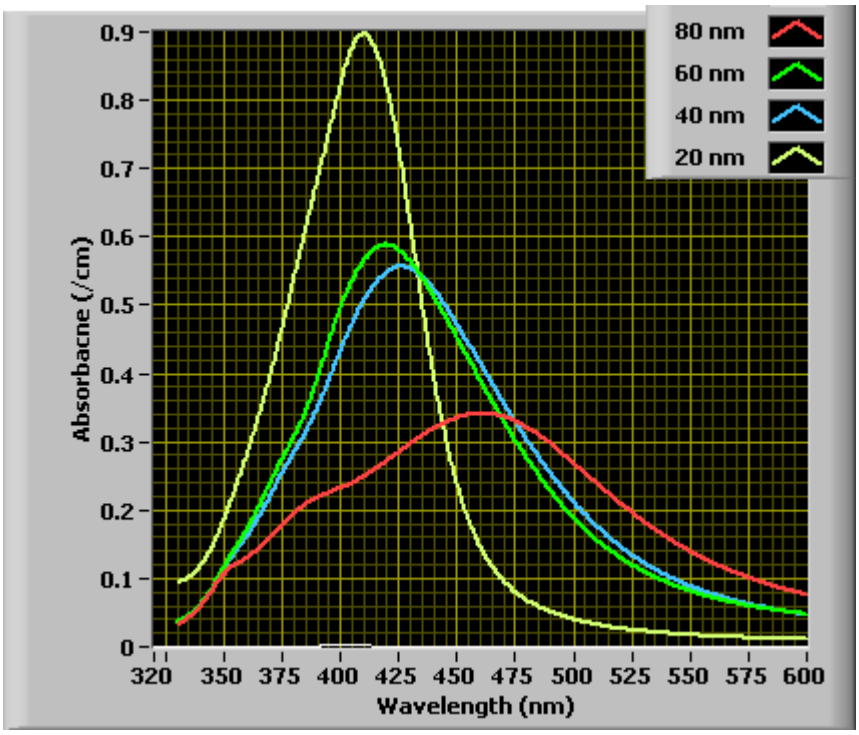

Figure 64. Absorbance spectra for 20, 40, 60 and 80-nm Ag nanoparticles surrounded by the air. The picture is reproduced from [25].

The spin-coating method has been used only for Ag nanoparticles being applied on the ITO surface and on the PEDOT:PSS surface. This geometrical configuration has been mentioned in part 4.1.1. Otherwise, direct mixing of colloidal Ag nanoparticles with the PEDOT:PSS or P3HT:$PCBM_{(60)}$ solutions would completely change the final chemical and physical properites of the layers. Before the fabrication of the structures, several series of experiments focused on the uniform spreading of Ag nanoparticles in the layers were performed. Since the Ag nanoparticles are immersed in water, they spread non- uniformly during the spin-coating. As a result, Ag nanoparticles agregate rather at the edge of the substrate which is unacceptable for us. Nevertheless, this problem has been succesfully solved. By using the hydroxypropyl cellulose (figure 65), the viscosity of aqueous solution containing the 20-nm nanoparticles has increased. The concentration of the used hydroxypropyl cellulose in the solution of colloidal Ag nanoaprticles was about 20 mg/mL. This concentration has provided a required viscosity of the aqueous solution with Ag nanoparticles. Consequently, the solution of the colloidal Ag nanoparticles has a form of a gel. The hydroxypropyl cellulose is generally available in the form of a white powder.

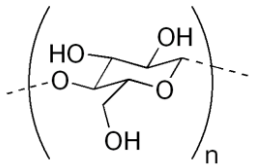

Figure 65. Molecular structure of the hydroxypropyl cellulose.

The created gel containing the hydroxypropyl cellulose and colloidal Ag nanoaprticles has been spin-coated at 500 rpm for one minute. Afterwards, the substrates have been put into an oven for baking at 300 °C for 20 minutes. At this temperature, all organic residues are removed and only Ag nanoparticles have rested intact. However, it is necessary to be aware of glass fragility at the baking process. After the substrates are cooled down to room temperature, it is possible to continue in the spin-coating of PEDOT:PSS and P3HT:$PCBM_{(60)}$ and in the evaporation of LiF/Al in the glove box. A schematic of the spin-coatin process is illustrated in figure 66.

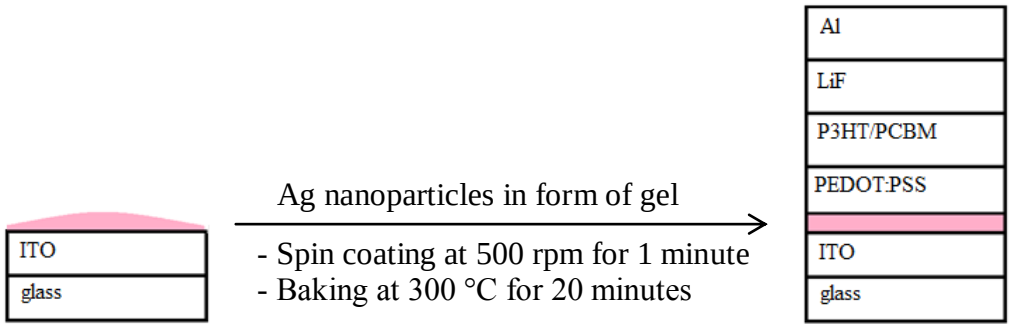

Figure 66. Deposition of colloidal Ag nanoparticles on ITO by spin-coating.

To understand well the importance of the baking process, the optical absorption of some samples before and after baking has been measured. Some samples with Ag nanoparticles in cellulose have been baked, whereas the others not. Figure 67 displays the difference between the baked (black line) and non-baked (red line) samples. It is evident, that the absorption of baked substrates is higher compared to the unbaked samples. In addition, it is worth noting that the unbaked system exhibits the negative absorption above 435 nm. This fact can be linked to resonant effects related to Ag. For Ag, plasmon resonances occur at the wavelength around 430 nm. As the result, a photoluminiscent effect can occur. Several studies have shown that interactions between plasmons and photogenerated excitons result in an enhanced exciton dissociation while suppressing bimolecular recombinations [26].

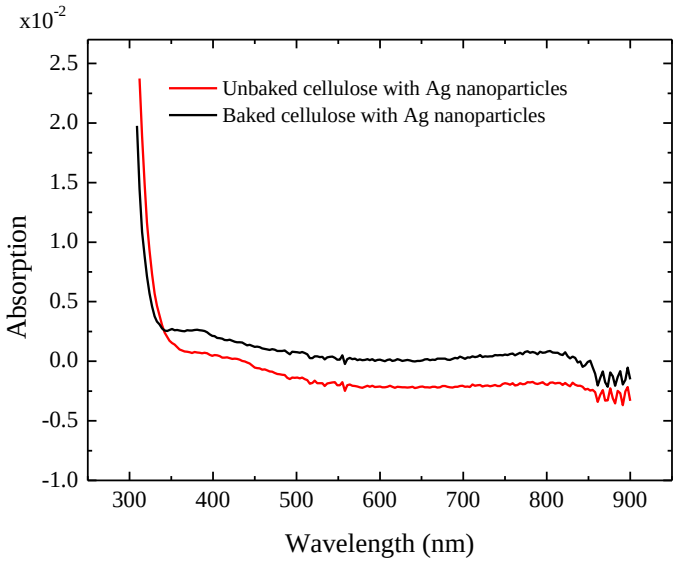

Figure 67. Absorption of baked and unbaked samples consisting of colloidal 20-nm Ag nanoparticles in form of gel. The higher absorption for the baked substrates is evident.

After the fabrication process atomic force microscopy method (*AFM*) of the samples with the spin-coated gel containing 20-nm Ag nanoparticles has been measured. The *AFM* image demonstrating the morphology of the baked sample with 20-nm Ag nanoparticles is shown in figure 68.

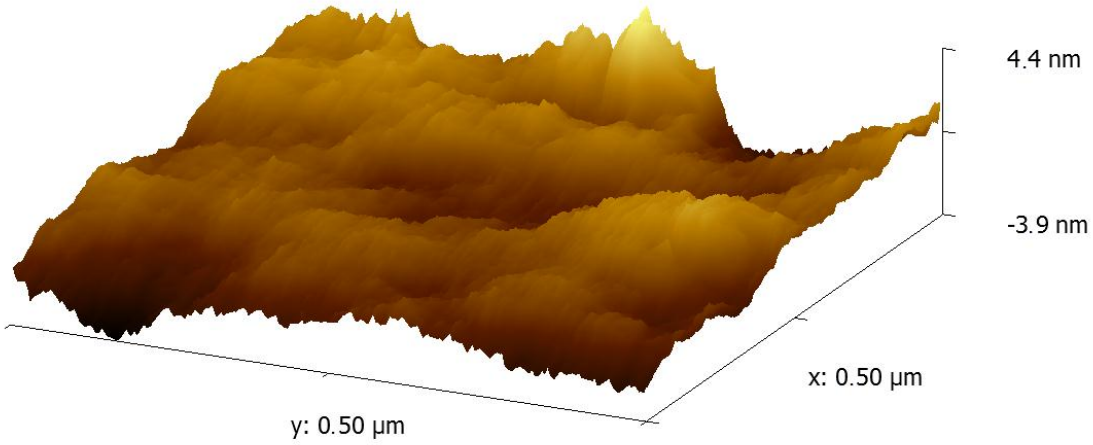

Figure 68. Morphology of the samples prepared by spin-coating usng a gel containing 20-nm colloidal Ag nanoparticles. This image has been taken by *AFM* in the non-contact mode.

5.1.3. Fabrication of samples modified with Ag nanoparticles – Drop-casting method

The drop-casting method represents a simple and effective technique of depositioning the colloidal Ag nanoparticles on the glass substrate. Compared to the spin-coating, the drop casting technique does not require any material modifications such as using the hydroxypropyl cellulose. In addition, by the drop-casting method, Ag nanoparticles can be put into a specific point on the substrate which represents another advantage. However, there is one step that must be taken into account at processing. The solution and substrates with colloidal Ag nanoparticles should be warmed up so that the water contained in the aqueous solution could simply evaporate. In our case, the aqueous solution with colloidal Ag nanoparticles has been warmed up to 80 °C and substrates up to 150 °C. Furthermore, the drop-casting method has been used for two configurations with Ag nanoparticles. These arrangements are shown in figure 69 and 70.

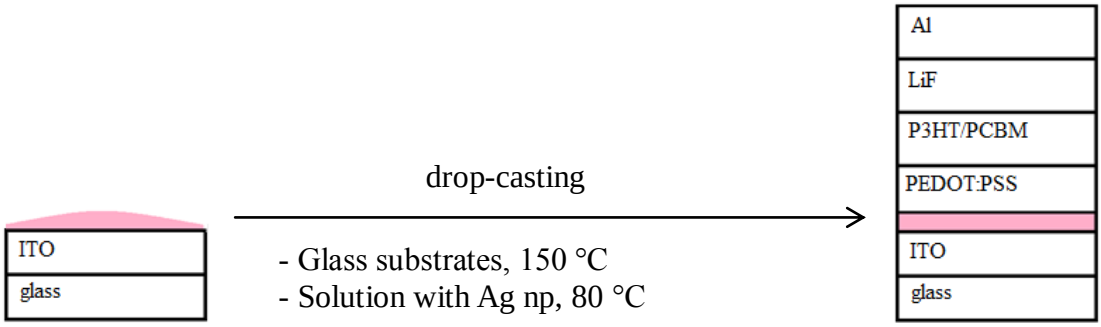

Figure 69. Drop-casting on the ITO surface. In total, five drops have been applied (one drop per minute). In this way, the evaporation of the residual water, contained in the solution with Ag nanoparticles, is assured.

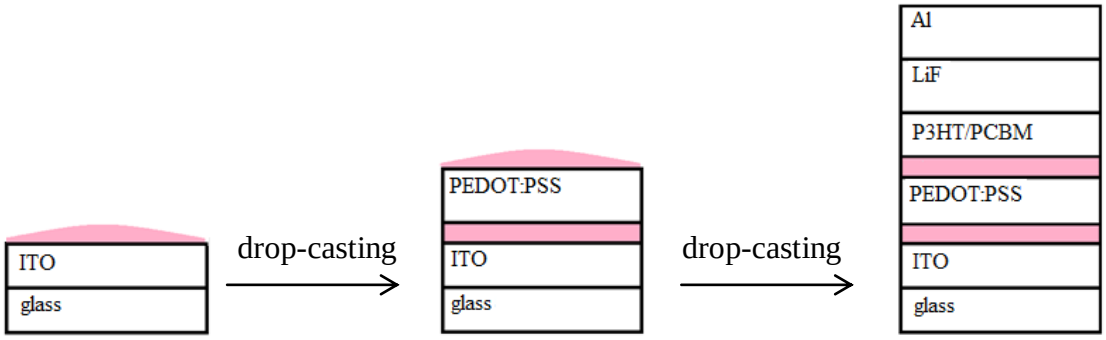

Figure 70. Drop-casting both on the ITO and PEDOT:PSS surfaces. For each surface, 5 drops have been applied (one drop per minute). Since the layer P3HT:$PCBM_{(60)}$ is hydrophobic, it is not possible to mix the aqueous solution containing Ag nanoparticles together with P3HT:$PCBM_{(60)}$. One of the possible solutions is to drop the colloidal Ag nanoparticles on the layer PEDOT:PSS which is not hydrophobic and let the water evaporate. This procedure should ensure a good contact between the Ag nanoparticles and the photoactive layer. Also here in this case, the glass substrates with ITO have

been warmed up to 150 °C and the solution containg colloidal 20-nm Ag nanoparticles to 80 °C.

The optical absorption has been measured also for samples prepared by this method. The results from this measurement are illustrated in figure 71, where the absorption of the drop-casted film is represented by the solid black line and the spin-coated film is represented by the solid red line. It is evident, that the absorption of the drop-casted substrates is higher at the wavelength range about 375-465 nm. It is also worth reminding that at 428 nm, the plasmon resonance effects occur for Ag. On the other hand, the samples performed by spin-coating exhibit the higher absorption above 465 nm. Further, for the drop-casted substrates, the negative absorption for the wavelengths below 306 nm is steel present. The noise that occur at higher wavelengths can be explained by interference effects.

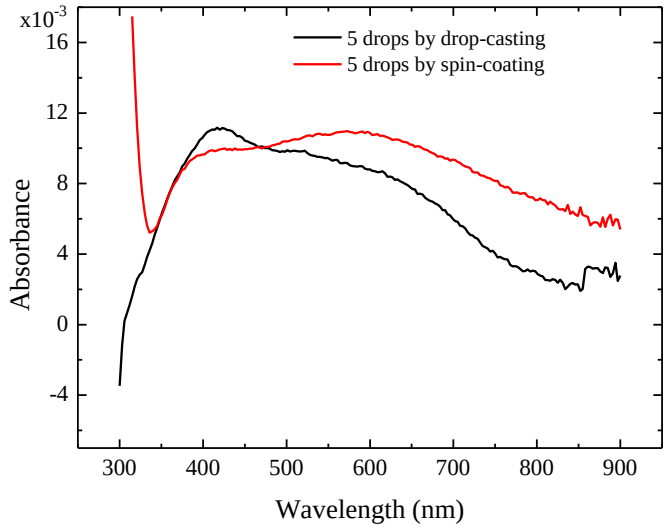

Figure 71. Absorption of drop-casted (black line) and spin-coated (red line) samples containing the layer of Ag nanoaprticles. Here, in both cases, the temperature of substrates has been kept at 150 °C and the temperature of the solution containg 20-nm Ag nanoparticles at 80 °C. Five drops have been consecutively applied (one drop per minute).

Despite the fact that the drop-casting is a local method, the Ag nanoparticles are supposed to be randomly dispersed even in the applied drop. In this method also a slower drying of the film in a solvent-saturated atmosphere occur. As the result, inhomogeneities in layer morphology cause unpredictable changes in electrical conductivity.

5.1.4. Fabrication of samples with deposited Ag nanoparticles.

The deposition method is the most promising technique how to get Ag nanoparticles on a substrate. This method requires a more complex setup such as vacuum and deposition chambers. This method provides a certain control of the size and distribution of Ag islands on the substrate. By appropriate setting of the deposition pressure, growth rate and deposition time, it is possible to control the Ag arrangement. However, for

technical reasons it was not possible to fabricate the samples by this method. The available equipement has enabled to deposit Ag on glass substrates only with dimensions about 10 x 10 mm, which does not correspond to the needed sample dimensions about 30 x 30 mm. Deposited substrates have been prepared in cooperation of Ing. Jindřich Mach, Ph.D.

It is required to cover substrates uniformly with Ag nanoparticles, as shown in figures 72 and 73. In principle, the best shape of these particles is represented by a cylinder or hemisphere because of their higher light scattering and trapping ability [10]. However, in our experiments, only colloidal Ag nanoparticles have been available.

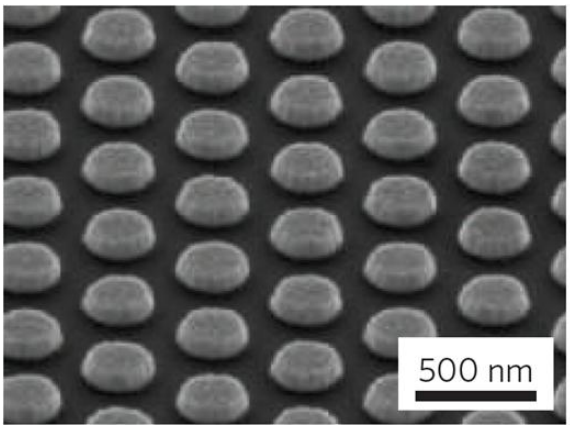

Figure 72. Hexagonal array of Ag nanoparticles deposited using the substrate conformal imprint lithography by the SCIL technique [10]. The particle diameter is about 300 nm. This image is made at an inclined perspective.

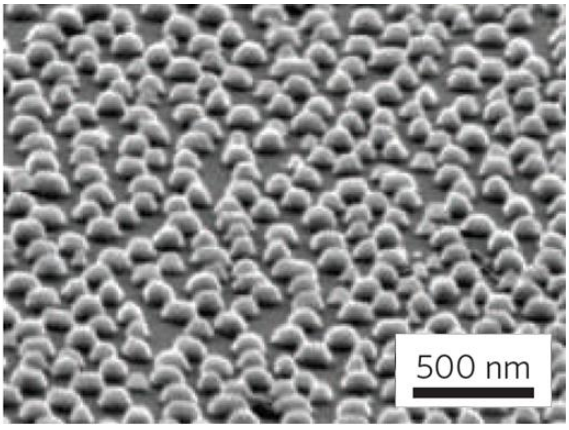

Figure 73. Silver nanoparticles evaporated through a porous alumina template, annealed at 200 °C [10]. The average particle diameter is about 135 nm. This image is made at an inclined perspective.

The deposition of Ag at least on substrates with dimensions about 10 x 10 mm has been performed. This has been done in order to see the distribution and size of deposited Ag islands. These islands are created from Ag layer approximately at 400 °C. Figures 74 and 75 illustrate the distribution and size of Ag islands by deposition at 400 °C for 15 minutes. The pressure in the vacuum chamber has been established at $2.7 \cdot 10^{-6}$ Pa.

However, there are some difficulties related to this method. At 400 °C, the morphology and the conductivity of ITO layer dramatically and irreversibly changes. For polymer photovoltaic solar cells, physical and morphological properties of ITO layer represent the very important factor. It has been also shown, that at 400 °C, tin and indium segregate on the substrate surface. These changes are shown in figures 76 and 77. Deposition conditions were the same as described above. The images 74-78 are made by scanning electron microscopy (SEM, TESCAN–MIRA 3[4]) with the kind assistance of Mgr. *et* Ing. Tomáš Šamořil.

[4] http://www.tescan.com/product.php?id_menu=27&id=24&name=MIRA+3+LM

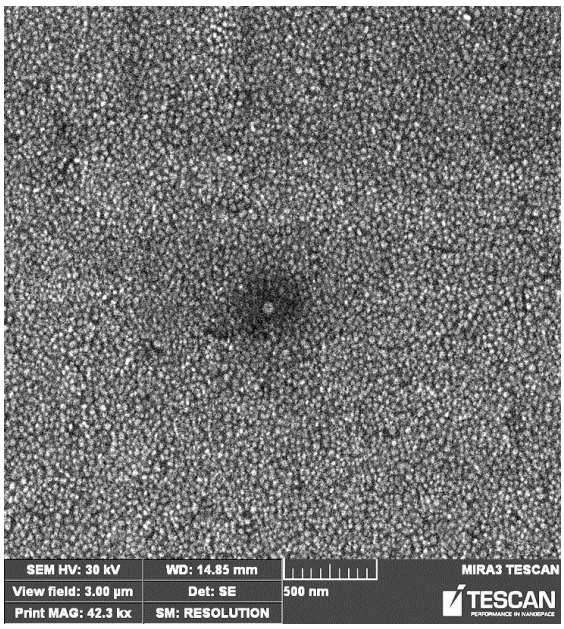

Figure 74. Deposited Ag islands. The small spot in the center is caused by an impurity or by a morphological defect on the glass substrate, (scale 500 nm).

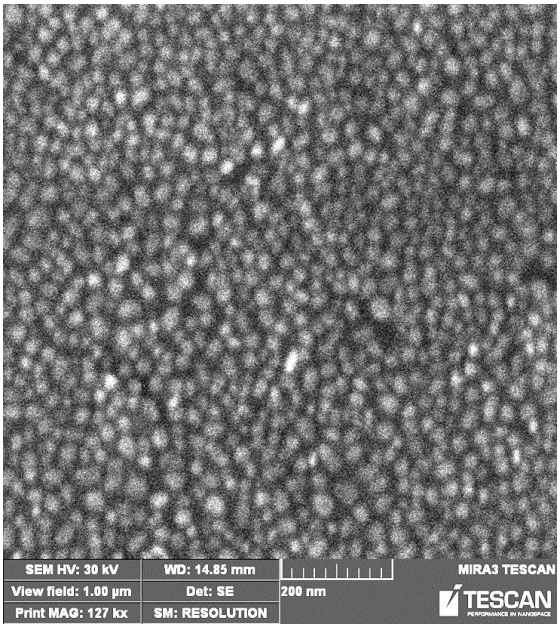

Figure 75. Deposited Ag islands. Here, the distribution and size of Ag islands meets the requirementsis (scale 200 nm).

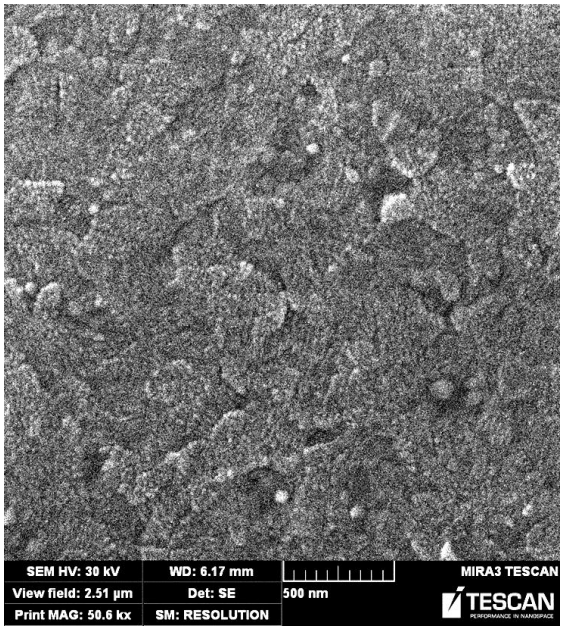

Figure 76. ITO on the glass substrate. ITO layer exhibits a furfuraceous morphology as seen above. This substrate does not contain deposited Ag.

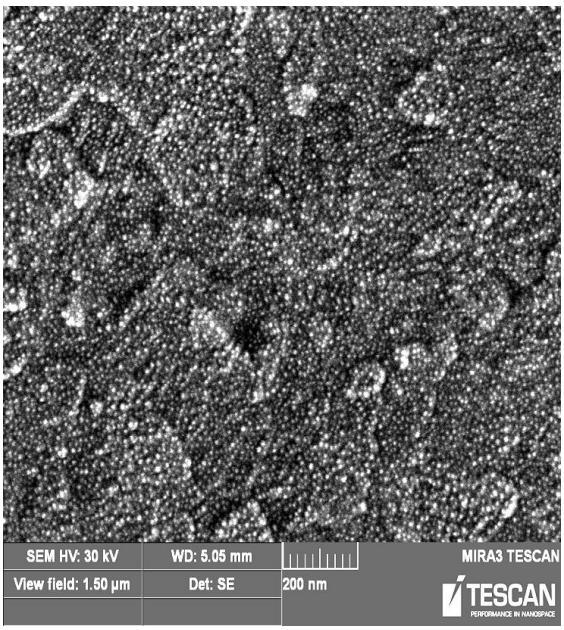

Figure 77. ITO on the glass substrate with Ag deposited at 400 °C. It is possible to see the modification of the original ITO morphology. Small bright points on the surface are supposed to be deposited Ag islands or Sn/In island that segregate from the bulk of ITO.

ITO is composed of In_2O_3 (90%) and SnO_2 (10%). As no detailed composition of ITO substrate after Ag deposition at 400 °C has been known, the energy dispersive spectroscopy (EDS) has been performed. By this method, the quantitative analysis of the elemental composition of a studied material can be done[5]. This analysis has been performed with the kind assistance of Ing. Drahomíra Janová. The results of the EDS measurements are summarized in figure 78 and in table 3.

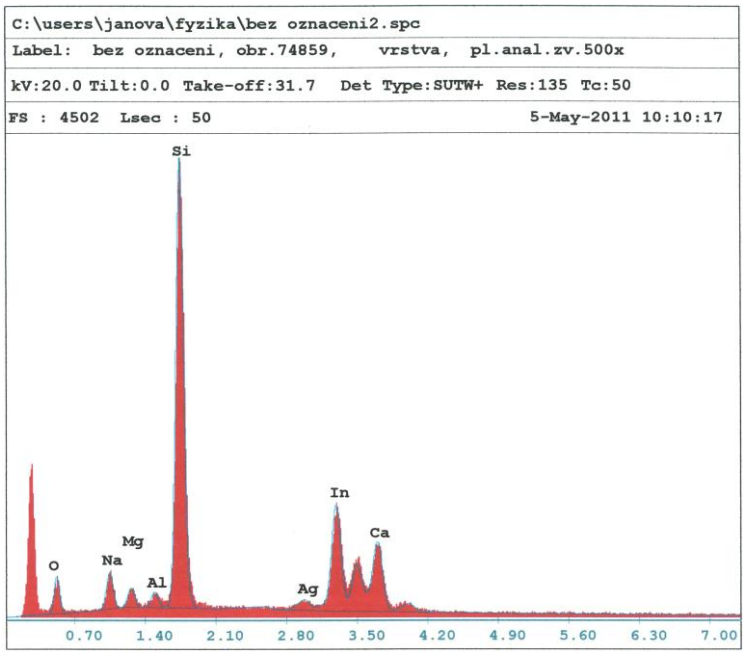

Figure 78. Representative EDS spectrum of Ag deposited at 400 °C at ITO glass substrate. The peak of Ag is visible, together with In. The concentration of Sn was under detection limits of this method.

EDAX ZAF Quantification (Standardless)
Element Normalized
SEC Table : Default
Coating Correction Used : Element : C , Factor : 14.00

Element	Wt %	At %	K-Ratio	Z	A	F
O K	20.04	38.61	0.0339	1.0952	0.1544	1.0004
NaK	5.32	7.14	0.0167	1.0244	0.3045	1.0035
MgK	2.09	2.65	0.0086	1.0499	0.3922	1.0065
AlK	1.38	1.58	0.0072	1.0188	0.5066	1.0118
SiK	33.32	36.58	0.2180	1.0482	0.6218	1.0039
AgL	2.41	0.69	0.0191	0.8431	0.9319	1.0045
InL	28.96	7.78	0.2346	0.8279	0.9783	1.0000
CaK	6.48	4.98	0.0586	1.0241	0.8836	1.0000
Total	100.00	100.00				

Element	Net Inte.	Bkgd Inte.	Inte. Error	P/B
O K	41.66	4.72	2.43	8.83
NaK	46.54	14.10	2.63	3.30
MgK	25.52	16.56	4.24	1.54
AlK	21.50	18.28	5.01	1.18
SiK	613.44	15.76	0.59	38.92
AgL	16.38	13.70	5.71	1.20
InL	184.42	13.78	1.12	13.38
CaK	105.40	12.26	1.53	8.60

Table 3. Percentage representation of elements measured on the ITO glass substrate with Ag deposited at 400 °C. These values have been acquired by the EDS method.

[5] http://www.edax.com

To summarize this section, five series of samples with different configurations have been made. To decrease measurement uncertainities, four samples for each configuration have been fabricated. One representative sample for each configuration is presented in table 4. The results from the measurements of these configurations are discussed separately below.

method	N° sample	configuration
reference	11	glass/ITO/PEDOT/P3HT:PCBM/LiF/Al
1	1	glass/ITO/Ag in gel/PEDOT/P3HT:PCBM/LiF/Al
2	3	glass/ITO/Ag drop/PEDOT/P3HT:PCBM/LiF/Al
3	14	glass/ITO/PEDOT/Ag drop/P3HT:PCBM/LiF/Al
4	10	glass/ITO/Ag drop/PEDOT/Ag drop/P3HT:PCBM/LiF/Al

Table 4. Different modifications comprising Ag nanoparticles.

Although, the devices prepared by vacuum deposition methods have not been realized for the device fabrication, they represent a big challenge for future experiments in photovoltaics.

5.2. Measurement technique

In this section, all measuring methods for finding required caracteristics of devices are described. Especially, the attention is paid to the measurement of volt-amper characteristics (*I-U*), external quantum efficiency (*EQE*), steady-state differential current (*SSDC*), layer thickness and morphology of prepared samples. The two last methods were executed directly in the air where the substrates degrade very fast. That is why these experiments were performed at the end of all the measuring processes. All the measurements were performed at room temperature (~25°C) and under the normal pressure (1013 hPa). Particular measuring setups are described separately below.

5.2.1. Volt-amper characteristics measurement (*I-U*)

The generation of charges is one of the key steps in photovoltaic devices during the conversion of the light into electrical energy. In most organic solar cells, the charges are created by the photoinduced electron transfer. Before *I-U* measurements, it is useful to anneal the devices based on P3HT:PCBM. This is made in order to increase the electron and hole mobility (figure 6). The *I-U* measurements were performed in a glove box filled with the inert gas N_2. During these experiments, the samples were exposed to the white light from a halogen lamp. The incident light power was 1000 W/m^2 and the measurement was performed under AM1.5 of the light spectral distribution (the spectrum of sunlight after passing 1.5 times through the thickness of the atmosphere) [3]. This imposes the important condition to the efficient charge generation. The device pattern contains four different areas to be measured (figure 79a). The dimensions of these areas are known. The *I-U* measurement was performed by two contacts for setting

the potential difference between two electrodes. The first contact is connected to the Al electrode, where negative charges (electrons) are collected and the second contact is applied to the ITO electrode, where positive charges (holes) are gathered. Then, there is the photoactive layer and PEDOT:PSS between the ITO and Al electrodes. Geometrical shapes and sizes of the ITO and Al electrodes are identical but rotated by 90° against each other (figure 79b). To contact the ITO layer, it is necessary to remove the photoactive and PEDOT:PSS layer. This is performed either by a mechanical way (scratching) or chemically. In the latter case, chloroform is used to eliminate the photoactive layer and aceton to remove the PEDOT:PSS layer.

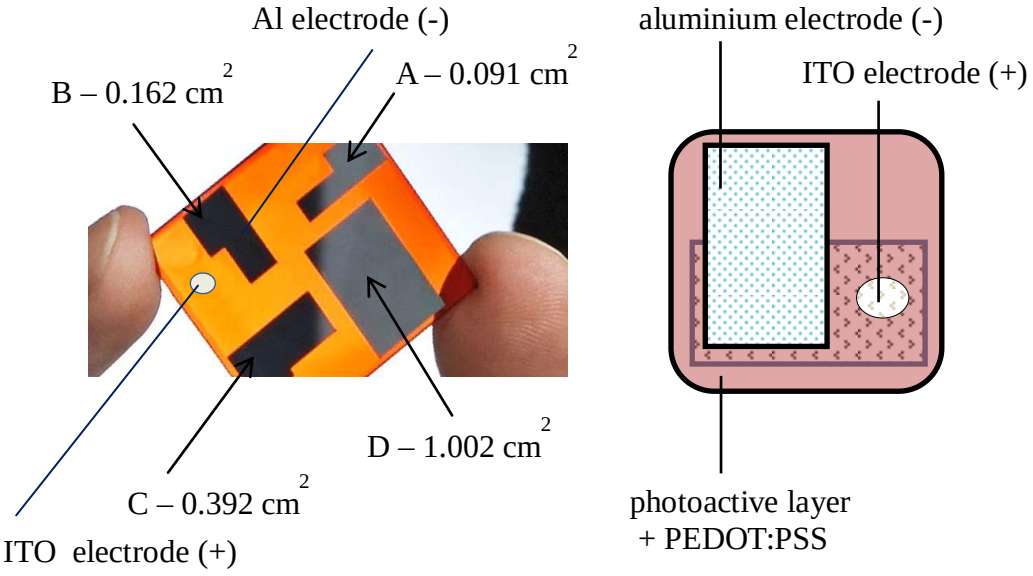

Figure 79. a) Architecture of the finished polymer photovoltaic sample [5]. Dimensions of the sample are (30 x 30) ± 1 mm and the thickness is about (0.5 ± 0.1) mm. **b)** Orientation of the ITO and Al electrodes in the polymer photovoltaic cell.

As *I-U* caracteristics are acquired over over the known A, B, C or D areas and the measured current is directly converted into the current density. From the *I-U* measurements, we get *I-U* curves such as those plotted in figure 80 and 81. These curves are important to the determination of the device power conversion efficiency η which is calculated by using equations 15a and 15b:

$$\eta = \frac{V_{\max} \times J_{\max}}{P_{IN}} = \frac{V_{OC} \times J_{SC} \times FF}{P_{IN}}, \tag{15a}$$

where

$$FF = \frac{V_{\max} \times J_{\max}}{V_{OC} \times J_{SC}} < 1. \tag{15b}$$

FF is the fill factor which is given by the ratio of the power obtained from the measurement (solid line rectangle in figure 80) and the maximum power (dashed line

rectangle in figure 79), P_{IN} is the incident light intensity (1000 W/m^2), J_{SC} is the short-circuit current density at zero applied voltage while illuminating, V_{OC} is the open-circuit voltage. V_{OC} is the maximum voltage that can be supplied by a device at $J = 0$ A/m^2. In principle, the more the shape of the measured *I-U* curve becomes rectangular, the more efficient the sample is. These values are acquired from the graph in figure 80. For the *I-U* curves measured in dark, three different regions are remarkable (figure 81). At low voltage from -1 V to 0.25 V, the measured current is dominated by the local leakage current. Weak spots in the film result in the ohmic behavior. In the range of 0.25 V to 0.8 V, the current increases exponentially with the applied voltage. In the range of 0.25 V to 0.8 V, the increase of the current is dominated. When the flat band condition is reached, the current becomes space-charge limited (drift dominated) [27].

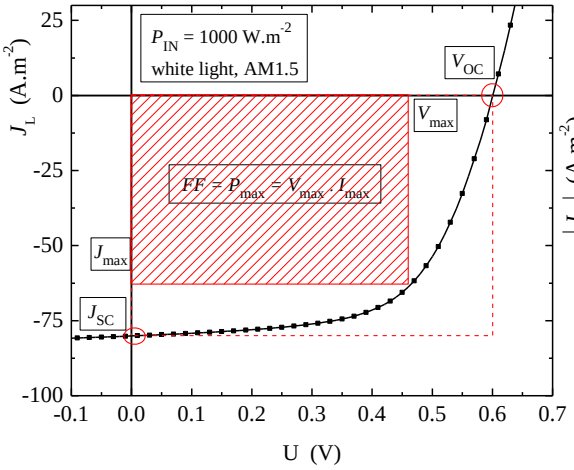

Figure 80. *I-U* curve measured under illumination (*L*) by the halogen lamp with the light power 1000 W/m^2.

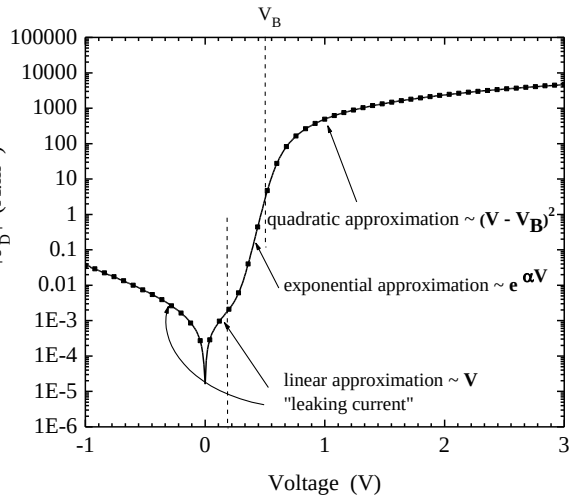

Figure 81. *I-U* curve measured without illumination (*D*).

Even if sixteen samples with different Ag modifications have been fabricated, only five representative samples with different Ag configurations are presented further. These results are shown in figure 82. For these series of the samples, the enhancement in J_{SC} is observable only for the configuration with 20-nm Ag nanoparticles dropped on the layer ITO (sample 3, solid green line). One of the possible explanations of this result is that Ag nanoparticles are concentrated in a drop and then there is a high increase in the electric intensity around these nanoparticles under illumination. On the other hand, the concentration of Ag nanoparticles in gel is not so high because of their uniform spreading. The smples 10 and 14, having the Ag nanoparticles into the photoactive layer, exhibit a linear behaviour. Therefore, these configurations appear rather conducting than exciton creating. This could be explained by too higher concentration of Ag nanoparticles in these layers which causes that the light is not able to come sufficiently through these layers. This could lead to a suppression of the exciton generation. On th eother hand, simulations of 20-nm Ag nanoparticles immersed in the photoactive layer show an enhancement in the absorption. However, 20-nm Ag nanoparticles immersed in the photoactive layer being thick only 60 nm represent a kind of the potential barrier during exciton formation.

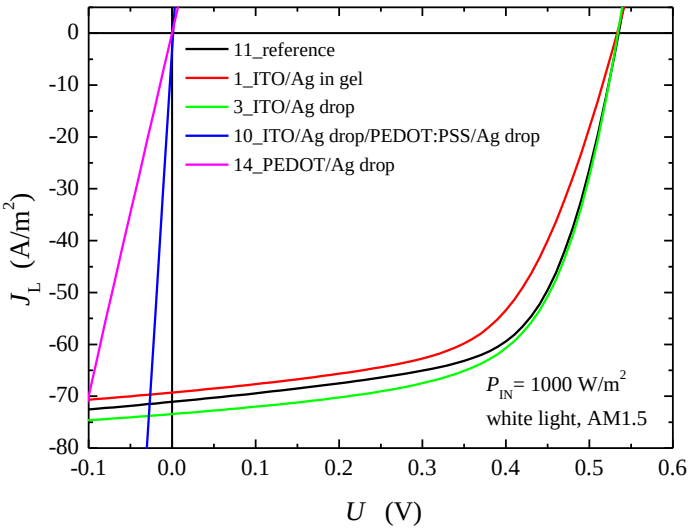

Figure 82. *I-U* curves measured under illumination for five different configurations. The enhancement in J_{SC} is observable only for the sample 3 with Ag nanoparticles dropped on the ITO layer.

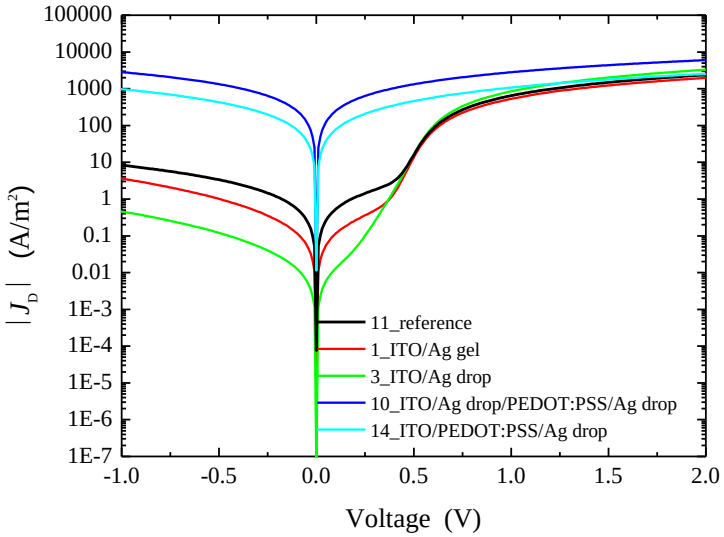

Figure 83. *I-U* curves measured without illumination for five different configurations. At the low voltage from -1 V to 0 V, the measured current is dominated by a local leakage due to weak spots in the blend, giving rise to the ohmic behavior. In the range of 0 V to 0.5 V, the current increases exponentially with voltage and above 0.5 V the current exhibits a quadratic behaviour.

The results achieved by *I-U* measurements at the samples modified with colloidal Ag nanoparticles are summarised in table 5.

N° sample	configuration	*FF*	*Jsc* (A/m^2)	*Voc* (V)	η (%)
11	reference	0.65	71.7	0.53	2.48
1	ITO/Ag in gel	0.59	68.9	0.53	2.14
3	ITO/Ag drop	0.63	73.4	0.53	2.43
10	ITO/Ag drop/PEDOT/Ag drop	-	-	-	-
14	ITO/PEDOT/Ag drop	-	-	-	-

Table 5. *I-U* characteristics of the samples modified with Ag nanoaprticles. Ag modifications of the samples are expressed in an abbreviated form.

5.2.2. External quantum efficiency measurement (*EQE*)

The external quantum efficiency method (*EQE*) is used to measure the current generated by the device per incoming photon (equation 16). It represents the electrical sensitivity of the device to the incoming light wavelength. Since the energy of a photon depends on the light wavelength, *EQE* is automatically measured over a wavelength range.

$$EQE = \frac{Number\ of\ electrons\ /\ \sec}{Number\ of\ photons\ /\ \sec} = 1240 \times \frac{J_{SC}}{P_{IN} \cdot \lambda}, \tag{16}$$

where J_{SC} is the short-circuit current density (in our experiments usually calculated over the area A = 0,091 cm^2), P_{IN} is the incident light power and λ is the wavelength of incident photons.

EQE setup (see in figure 84) is composed of a halogen lamp which provides white light (U_{lamp}= 12 V, I_{lamp}= 4,3 A), chopper transforming the light into a pulsed signal ($f_{chopper}$ = 170 Hz), monochromator that selects particular wavelengths, system of lenses (L), sample or silicon diode for calibration. The signal is measured by a lock-in amplifier or multimeter (calibration). First, the light intensity is measured by the reference silicon diode. The curves acquired from the *EQE* measurements are shown in figure 85. Once the certain quantity of photons is absorbed in the photoactive layer, the exciton is created. In this way, an electron-hole pair is formed. These charges need to be separated and collected on the electrodes. A "good" material avoids the bimolecular recombination and therefore exhibits a peak in the external quantum efficiency [5].

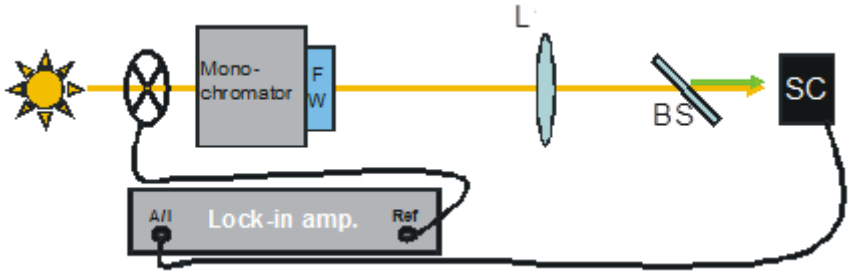

Figure 84. *EQE* setup. BS-beam splitter, SC-reference silicon diode or solar cell sample

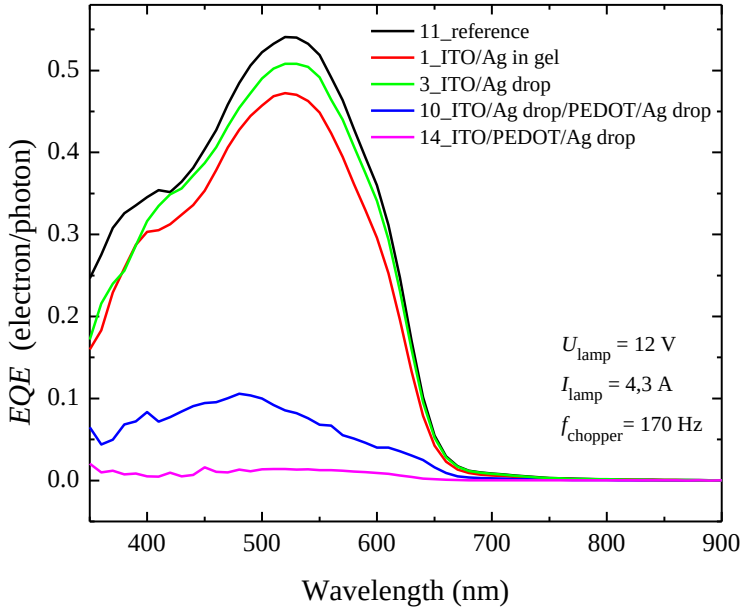

Figure 85. *EQE* measurements.

Even if the sample 3 in figure 82 exhibits the enhancement of J_{SC} compared to the reference cell (figure 82), in figure 85, all the samples show the lower EQE than the reference sample. However, all the curves have at least a small peak for the wavelengths around 420 nm which is the wavelength where the plasmon resonance effects for Ag nanoparticles occur. Otherwise, the majority of organic solar cells are sensitive to the wavelength about 532 nm (green color) where the exciton creation is the most efficient.

5.2.3. Steady-state differential current measurement (*SSDC*)

The steady-state differential current measurement (*SSDC*) is relatively a new method to determine losses during the charge carrier transport. The *SSDC* setup is composed almost of the same components as the *EQE* one. But in *SSDC*, there is a laser working at the wavelength 532 nm and an optical density filter (OD_n) changing the intensity of the laser beam, additionally. The response of the sample to the light intensity coming simultaneously both from the laser and the halogen lamp is detected. The *SSDC* setup is shown in figure 86.

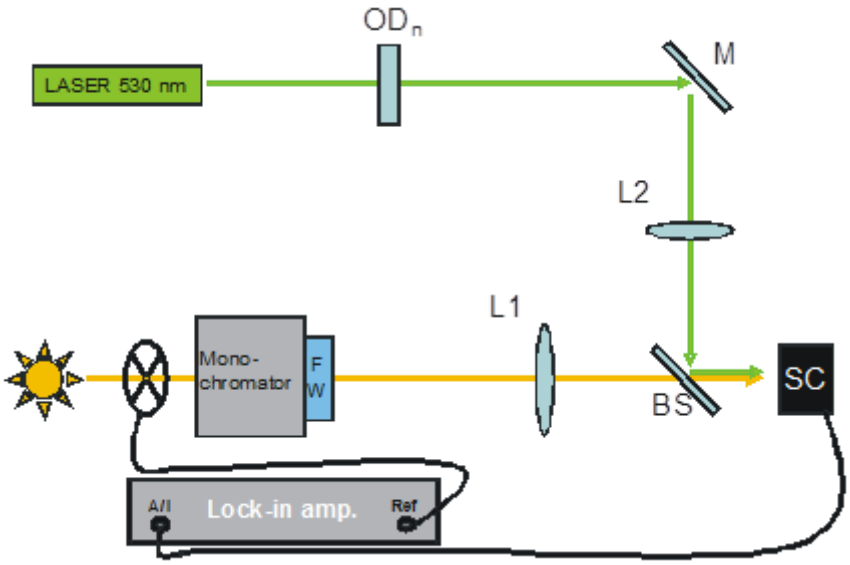

Figure 86. *SSDC* setup. BS-beam splitter, SC-reference silicon diode or solar cell sample, OD_n-optical density filter. The other symbols are the same as in Fig. 84. The halogen lamp (U_{lamp}= 12 V, I_{lamp}= 4.3 A) provides the white light.

Before the measurement is started, it is necessary to calibrate the light intensity. For this purpose, the multimeter measures the simultaneous current response of the reference silicon diode to the laser light passing different optical density filters and to the light from the halogen lamp going through the monochromator set to the laser wavelength (532 nm - green colour). In this case the chopper of the light has been switched-off. Besides the availability of the laser working at the wavelength 532 nm the additional reason for choosing this wavelength was the fact the the organic solar cells and the human eye are the most sensitive to it. To measure the voltage response ΔU of the prepared solar cell to the incident light, the both halogen lamp and laser are switched-on. Under these conditions the chopper works at 170 Hz and the lock-in amplifier detects the voltage response ΔU to the incident light intensity being changed by optical density filters. As there is a resistance about 50 Ω installed in the lock-in amplifier, ΔU can be converted into ΔJ using equation 17:

$$\Delta J = \frac{\Delta I}{A} = \frac{\Delta U}{R \cdot A}, \tag{17}$$

where R is the resistance integrated in the lock-in amplifier and A is the area of the measured sample (figure 79a). Typical curves obtained from *SSDC* measurements are plotted in figure 87. As these curves exhibit a plateau for low intensities, it is reasonable to normalize them to this plateau value.

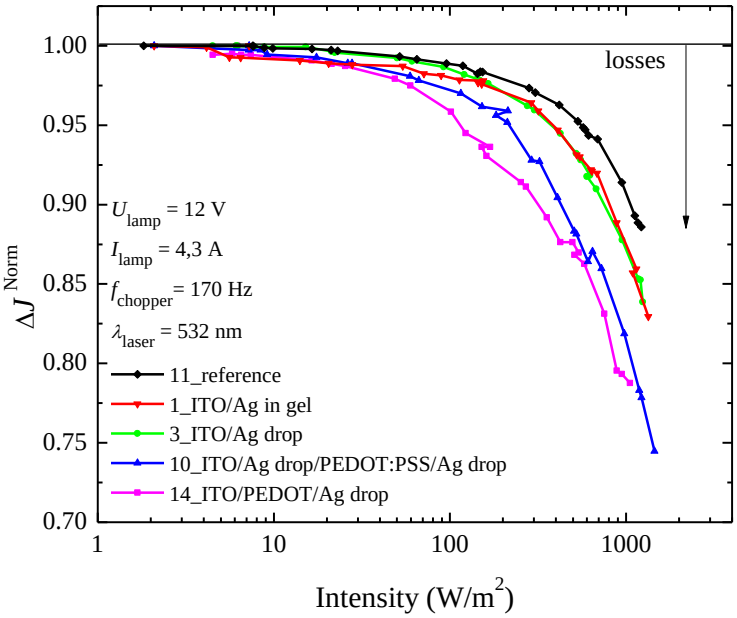

Figure 87. *SSDC* measurements. ΔJ decreases unproportionally with the light intensity. The black arrow represents the loss efficiency which is described by the relation $\xi = 1 - \Delta J^{Norm}$. If the loss curves exhibit linear behaviour, then the losses come from bimolecular recombinations.

In general, the losses in an organic photovoltaic device are significant for the higher incoming light intensity. Higher intensity results in the higher exciton generation. However, as more oposite charges are present, the probability of the recombination between these charges increases as well.

In addition, there is another way how to express the losses [27]. In this case, the losses are linked to the coefficient α which ranges typically from 0.85 to 1. The coefficient α expresses the relation between the short-circuit current density J_{SC} and the incident light intensity I (equation 18). It is typical for solar cells based on organic polymers, that the dependence between J_{SC} and I is not always exactly linear [3] (figure 88)

$$J_{SC} \propto I^{\alpha}. \tag{18}$$

The values of J_{SC} are measured under conditions when the halogen lamp is switched-off and the laser is switched-on. Here, a multimeter is used to determine the current response

of the solar cell to the light intensity coming from the laser through the system of optical density filters. The effort of scientific groups dealing with the improvement in organic photovoltaics is to approach the coefficient α close to one and thus to minimize losses in such devices. The nearly linear dependence of J on the incident light intensity in Fig. 88 suggests the absence of bimolecular recombinations and space-limited charges. The incorporation of Ag nanoparticles into the system does not affect the charge transport process in the device [26].

The losses are closely associated with electron and hole mobilities. It has been proved that the annealing of samples significantly improves the charge carrier mobility which results in a decrease of bimolecular recombinations (figure 7) [3].

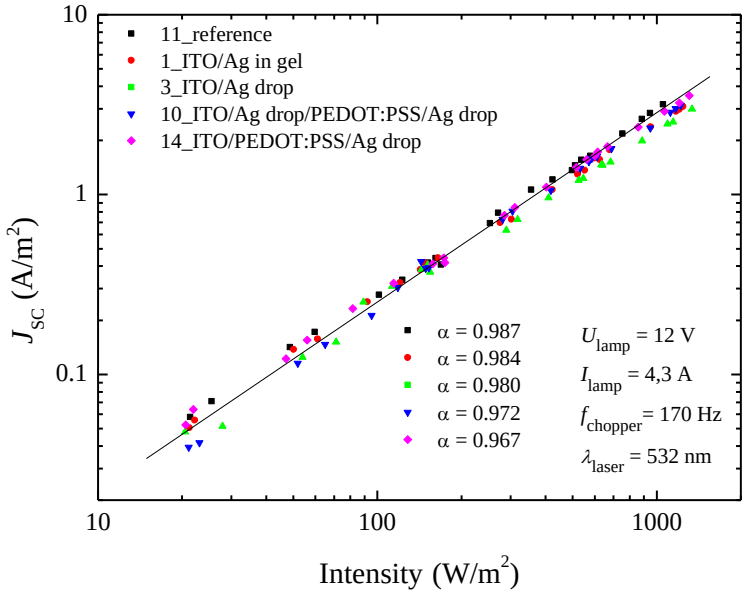

Figure 88. Dependance of the photocurrent density on the incident light intensity

5.2.4. Layer thickness measurement

After *I-U*, *EQE* and *SSDC* measurements, the thickness of the photoactive layer was measured. For this purpose, the profiler DEKTAK 150 was used. Before the measurement it was necessary to artifically create some surface diversities on the sample. This was done by scratching the sample. The available vertical resolution depends upon the selected range of the measurements. When measuring an extremely fine topography, the DEKTAK provides the vertical bit resolution 0.1 nm. For general applications, such as the measurement of the photoactive layer, the vertical resolution about 1 nm is adequate [28]. Since the measurement on th e DEKTAK 150 is realized directly at ambient atmosphere, where the samples are sensitive to fast degradation because of their oxydation, it is required to perform this kind of measurements at the end of all the procedures. The surface profilometer DEKTAK 150 is shown in figure 89[6].

[6] http://www.bruker-axs.com/dektak-150_stylus_profilometer.html

Figure 89. The surface profilometer DEKTAK 150.

It is important to keep in mind that for our samples, we measured total thickness that includes the layers as PEDOT:PSS and P3HT:PCBM$_{(60)}$. To get the real thickness of the photoactive layer, it is necessary to substract 50 nm from all the mesured values ($d = d_1 - 50$ nm). The layer thickness about 50 nm corresponds to the PEDOT:PSS layer prepared under conditions being discussed in Section 5.1.1. The layer thicknesses measured by this method are presented in Table 6.

N° sample	**configuration**	d_1 **(nm)**	d **(nm)**
11	reference	115	65
14	ITO/PEDOT:PSS/Ag-drop	111	61
10	ITO/Ag-drop/PEDOT:PSS/Ag-drop	110	60
3	ITO/Ag-drop	107	57
1	ITO/Ag in gel	104	54

Table 6. Thicknesses of the photoactive layer (d) for all the modifications.

Since all the layers PEDOT:PSS and P3HT:PCBM$_{(60)}$ have been prepared by the same processing method, it is possible to determine the average photoactive layer thickness. With 95% certainty the average photoactive layer thickness influenced by different Ag modifications inheres in the range of

$$\bar{d} = (59 \pm 6)\,\text{nm}\,.$$

5.2.5. Atomic force micoscopy measurement (*AFM*)

Atomic force microscopy has been performed at the very end of all the experiments. This kind of the measurements is done in order to know the morphology of produced samples. The determination of the morphology structure is a very important factor which can help us to better understand the physical properties of fabricated devices. In addition, the knowledge relating to sample morphology can lead to an improvement of individual processing steps that affect the power conversion efficiency. All the *AFM* measurements have been performed directly in the air and in the noncontact mode where the cantilever is oscilating with an amplitude of tens nanometers above the surface of the studied sample. This mode is less sensitive to the sample degradation than the contact mode. Figures 90 and 91 show *AFM* images of the sample based on P3HT:$PCBM_{(60)}$ and modified with 20-nm colloidal Ag nanoparticles. All the *AFM* measurements have been made by AUTOPROBE CP-II (VEECO), model no. AP-0100.

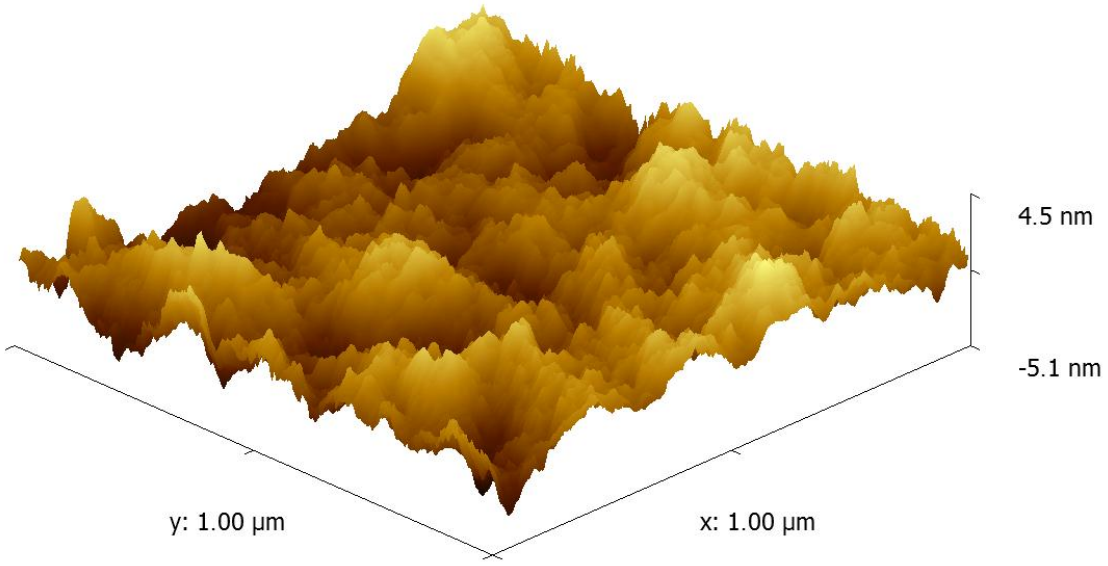

Figure 90. *AFM* image of the device surface based on P3HT:$PCBM_{(60)}$ (1:1). The sample is modified with 20-nm colloidal Ag nanoparticles dropped on the ITO layer.

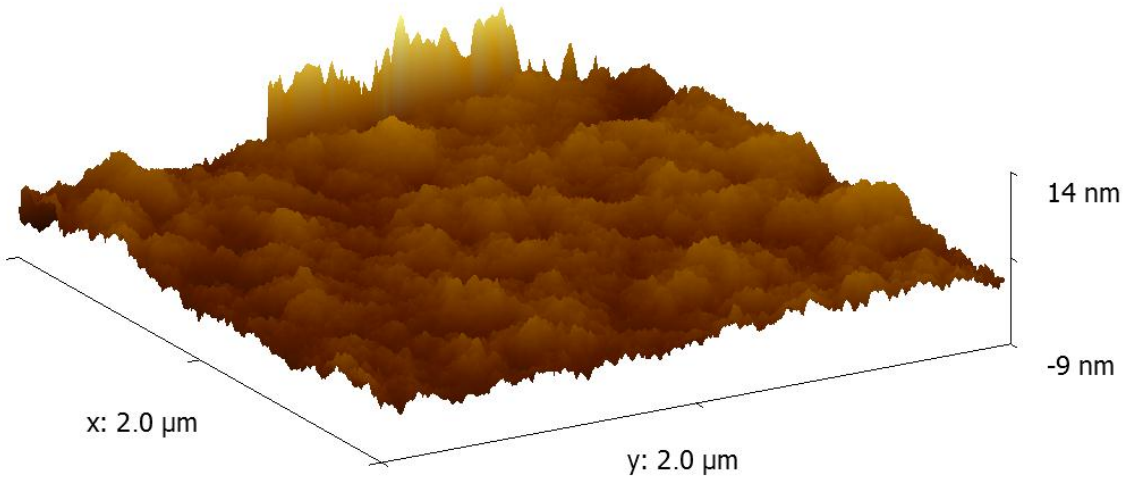

Figure 91. *AFM* image of the device based on P3HT:$PCBM_{(60)}$. The sample is modified with 20-nm colloidal Ag nanoparticles dropped on the ITO and on the PEDOT:PSS layer.

Even if the scales of both the presented images are not the same, it is clear that the roughness of the sample modified with 20-nm colloidal Ag nanoparticles dropped on the ITO and on the PEDOT:PSS layer is higher than the roughness of the sample where these nanoparticles are dropped only on the ITO layer.

6. CONCLUSION

The thesis deals with the application of plasmonics in organic photovoltaics. Briefly speaking, Ag nanoparticles have been put into P3HT:PCBM$_{(60)}$ based organic solar cells in order to enhance the absorption in their photoactive layer. (***i***) General discussions dealing with the organic photovoltaics have been done. (***ii***) Fundamentals of the application of the plasmonics in the organic photovoltaics have been mentionned. In this part, basic plasmonic effects leading to the enhancement in the absorption of polymer based solar cells have been also theoretically analysed. (***iii***) Numerical simulations used to study the electromagnetic effects in the vicinity of metal nanostructures have been performed. In this part, different geometrical arrangements of Ag nanostructures in polymer photovoltaic system have been analyzed. Simulations show that for Ag nanoparticles positionned in the photoactive layer, the highest enhancement in the absorption is observable. It is worth reminding that the P3HT:PCBM$_{(60)}$ layer is very sensitive to modest changes in its morphology, temperature and electromagnetic conditions. These parameters significantly affect the charge carrier mobility. Afterwards, the processing of the samples based on P3HT:PCBM$_{(60)}$ (1:1) is described in detail as well as their modification with 20-nm colloidal Ag nanoparticles. Ag nanoparticles have been incorporated either by spin-coating or drop-casting methods. For the spin-coated samples, viscosity of the solution containing 20-nm colloidal Ag nanoparticles has to increased to avoid the non-uniform spreading of colloidal Ag nanoparticles at spin-coating. For this purpose, the hydroxypropyl cellulose has been used. At the end, the measurements of volt-amper caracteristics (*I-U*), external quantum efficiency (*EQE*), steady-state differential current (*SSDC*), layer thickness and atomic force microscopy (*AFM*) have been performed. Only for the sample modified with 20-nm Ag nanoparticles dropped on the ITO layer the *I-U* measurements show an enhancement of the short-circuit current density J_{SC} while keeping its overal efficiency nearly at the same level. J_{SC} reaches 73.4 A/m^2 compared to 71.7 A/m^2 for the reference cell. The *EQE* measurement of this sample does not exhibit any dramatic improvement compared to the reference cell. These results might be explained by a nonuniform spreading of Ag nanoparticles in individual layers or by the insufficient photoactive layer thickness. For 20-nm Ag nanoparticles the photoactive layer thickness is only about 60 nm and could represent a kind of potential barrier for creation of excitons. On the other hand, the method based on the vacuum deposition of Ag nanostructures seems to be a promising method for the enhancement of the power conversion efficiency of organic solar cells. Unfortunately, for technical reasons this method could not have been tested and should become a subject of further research.

List of symbols and abbreviations used in this work:

ε'	real part of dielectric constant
ε''	imaginary part of dielectric constant
$\vec{k}$	propagation vector
$\|E\|^2$	square of magnitude of electric intensity
AFM	atomic force microscopy
Ag	silver
AM1.5	air mass 1.5
Au	gold
BHJ	bulk heterojunction
$c(r)$	specific heat
D	electric induction
d	layer thickness
E	electric intensity
E_B	binding energy
EDS	energy dispersive spectroscopy
EQE	external quantum efficiency
F	field strength
FDTD	finite-difference time-domain
FF	fill factor
GaAs	gallium arsenide
H	magnetic induction
HOMO	the highest occupied molecular orbital
I_{SD}	intensity of silicon diode
ITO	indium tin oxide
I-U	volt-amper characteristics
J_{max}	maximum current densit
J_{SC}	short-circuit current density
k	imaginary part of refractive index (extinction coefficient)
$k(r)$	thermal conductivity
k_r	recombination constant
LSPR	localized surface plasmon resonance
LUMO	the lowest unoccupied molecular orbital
n	real part of refractive index (extinction coefficient)
OPV	organic photovoltaics
OPVD	organic vapor-phase deposition
P3HT	Poly(3-hexylthiophene)
$PCBM_{(60)}$	[6,6]-Phenyl-C61-butyric-acid-methyl ester
PCED	pulse-current electrodeposition
PEDOT:PSS	poly(3,4-ethylenedioxythiophene):poly (styrenesulfonate)
P_{IN}	incident light intensity
PML	perfectly matched layer
q	elemntary charge
$Q(r,t)$	energy from light dissipation
r	spacial coordinates
SSDC	steady-state differential current

TOF	time of flight
V_{max}	maximum voltage
V_{OC}	open-circuit voltage
α	exponent in $J_{SC} \propto I^{\alpha}$
γ	field activation parameter
$\Delta T(r,t)$	local temperature
ΔT_{max}	maximum enhancement in temperature
μ_0	zero-field mobility
$\mu_{e\,(h)}$	electron (hole) mobility
ξ	losses
$\rho(r)$	mass density

BIBLIOGRAPHY

[1] Derkacs D. et al.: Improved performance of amorphous silicon solar cells via scattering from surface plasmon polaritons in nearby metallic nanoparticles *Applied Physics Letters* 89, 093103 (2006).

[2] Honsberg Ch., Barnett A.: UD-led team sets solar cell record, 2008. UDAILY - University of Delware. http://www.udel.edu/UDaily/2008/jul/solar072307.html (accessed Jan 30, 2011).

[3] Koster, L.J.A.; Device physics of donor/acceptor-blend solar cells. University of Groningen, The Netherlands, 2007. ISBN 9789036729413.

[4] Ströck, M.; et al. Fullerenes, 2007. Wikipedia. ttp://en.wikipedia.org/wiki/Fullerene (accessed May 21, 2011).

[5] Janssen, R.A.J.; Introduction to polymer solar cells (3Y28). Department of Chemical Engineering and Chemistry, Eindhoven University of Technology, The Netherlands. http://user.chem.tue.nl/janssen/SolarCells/Polymer%20solar%20cells.pdf

[6] Luxpop. Thin film and bulk index of refraction and photonics calculations. http://www.luxpop.com/ (accessed May 07, 2011).

[7] Zheng, X.; et al. Energy level alignment of poly(3-hexylthiophene): [6,6]-phenyl C61 butyric acid methyl ester bulk heterojunction. *Applied Physics Letters* **2009**, *95* (133), 1–3.

[8] Sariciftci, N.S.; Zhokhavets, U.; et al. Effect of annealing of poly(3-hexylthiophene)/fullerene bulk heterojunction composites on structural and optical properties. *Thin Solid Films* **2006**, (496), 679–682.

[9] Brinek, L. Plasmonic resonant antennas. Diploma thesis, Brno University of Technology, Faculty of Mechanical Engineering, Institute of Physical Engineering, Czech Republic, 2008.

[10] Atwater, H.A.; Polman A. Plasmonics for improved photovoltaics devices. *Nature Materials* **2010**, *9* (2529), 205–213.

[11] Hoppe, H.; Sariciftci, N.S.; Meissner, D. Optical constants of conjugated polymer/fullerene based bulk-heterojunction organic solar cells. *Mol. Cryst. Liq. Cryst.*, **2002**, *385*, 113–119.

[12] Tvingstedt, K.; Rahachou, A.; et al. Surface plasmon increase absorption in polymer photovoltaic cells. *Applied Physics Letters* **2007**, *91* (113514), 1–3.

[13] Kim, S.; Nah, Y.; et al. Plasmon enhanced performance of organic solar cells using electrodeposited Ag nanoparticles. *Applied Physics Letters* **2008**, *93* (073307), 1–3.

[14] Westphalen, M.; Meissner, D.; et al. Metal cluster enhanced organic solar cells. *Solar Energy Materials and Solar Cells* **2000**, *61*, 97–105.

[15] Kim, Ch.H.; Kotov, N.A.; Silver Nanowire Embedded in P3HT:PCBM for High-Efficiency Hybrid Photovoltaic Device Applications. *ACS NANO* **2011**, *5* (4), 3319–3325.

[16] Hägglund, C.; Kasemo, B. Nanoparticle Plasmonics for 2D-Photovoltaics: Mechanisms, Optimization, and Limits. *OPTICS EXPRESS* **2009**, *17* (14), 11944–11957.

[17] Govorov, A.O.; Richardson, H.H. Generating heat with metal nanoparticles. *Nano-today* **2007**, *2* (1), 30–38.

[18] Morfa, A.; Reilly III, T.; et al. Plasmon-enhanced solar energy conversion in organic bulk heterojunction photovoltaics. *Applied Physics Letters* **2008**, *92* (013504), 1–3.

[19] Palik E. D. *Handbook of Optical Constants of Solids*, 1st ed.; Academic Press inc., London, 1985. 103 p. ISBN 0-12-544424-9.

[20] Ng, A.M.C.; Wan, W.K.; et al. Spectroscopic ellipsometry characterization of polymer–fullerene blend films. *Thin Solid Films* **2008**, *517*, 1047–1052.

[21] Green, M.A.; Pillai, S. Plasmonics for photovoltaic applications. *Solar Energy Materials and Solar Cells* **2010**, *94*, 1481–1486.

[22] Catchpole, K.R.; Polman, A. Plasmonic solar cells. *OPTICS EXPRESS* **2008**, *16* (21793), 1–3.

[23] Benziger, J.; Forrest, S. Organic Vapor Phase Deposition for Optoelectronic Devices, 2007. Princeton. http://www.princeton.edu/~benziger/OVPD.pdf (accessed May 16, 2011).

[24] Lippert, T. Spin coating, 2009. Materials group of Paul Scherrer Institut. http://materials.web.psi.ch/Research/ThinFilms/Methods/Spin.htm (accessed May 17, 2011).

[25] Silver Colloid, 2011. BBInternational. http://www.bbigold.com (accessed May 22, 2011).

[26] Wu, J. L.; Hsu, Ch. S.; et al. Surface Plasmonic Effects of Metallic Nanoparticles on the Performance of Polymer Bulk Heterojunction Solar Cells. *ACS NANO* **2011**, *5* (2), 959–967.

[27] Mihailetchi, V. Device Physics of Organic Bulk Heterojunction Solar Cells. Ph.D. Thesis, University of Groningen, The Netherlands, 2005. ISBN 90-367-2393-0.

[28] Maier, S. *Plasmonics: Fundamentals and Applications*, 25th ed.; Springer, Heidelberg, Germany, 2007. 223 p. ISBN 978-0-387-33150-8.

[29] Raether, H. *Surface Plasmons on Smooth and Rough Surfaces and on Gratings*, 1st ed.; Springer, Berlin, Germany, 1988. 136 p. ISBN: 978-3540173632.